Bioactive Materials 50 (2025) 475–493

Contents lists available at ScienceDirect

Bioactive Materials

journal homepage: www.keaipublishing.com/en/journals/bioactive-materials

Sequential simulation of regeneration-specific microenvironments using scaffolds loaded with nanoplatelet vesicles enhances bone regeneration

Wenshuai Li [a,b,c,1], Qichen Shen [c,1], Tong Tong [a,b,1], Hongsen Tian [d,e], Xiaowei Lian [a,b], Haoli Wang [d,e], Ke Yang [d,e], Zhanqiu Dai [d,e], Yijun Li [f], Xianhua Chen [g], Qingqing Wang [d,e,i], Dan Yang [h], Feng Wang [a,b,*], Feng Hao [h,**], Linfeng Wang [a,b,***]

[a] Department of Orthopaedic Surgery, The Third Hospital of Hebei Medical University, Shijiazhuang, 050051, China
[b] The Key Laboratory of Orthopedic Biomechanics of Hebei Province, The Third Hospital of Hebei Medical University, Shijiazhuang, 050051, China
[c] Hangzhou OrigO Biotechnology Co. Ltd., Hangzhou, Zhejiang, 310016, China
[d] Department of Orthopaedic Surgery, Sir Run Run Shaw Hospital, Medical College of Zhejiang University, Hangzhou, Zhejiang, 310016, China
[e] Key Laboratory of Musculoskeletal System Degeneration and Regeneration Translational Research of Zhejiang Province, Hangzhou, Zhejiang, 310016, China
[f] The First Affiliated Hospital of Wenzhou Medical University, Wenzhou, Zhejiang, 325000, China
[g] Zhejiang Institute of Medical Device Testing, Hangzhou, Zhejiang, 310016, China
[h] Zhejiang DecellMatrix Biotechnology Co. Ltd., Hangzhou, Zhejiang, 310016, China
[i] Cixi Biomedical Research Institute, Wenzhou Medical University, Zhejiang, 315000, China

ARTICLE INFO

Keywords:
Bone regeneration
Scaffolds
Platelet vesicles
Decellularized cancellous bone matrix
Bone marrow mesenchymal stem cells

ABSTRACT

Bone regeneration is a complex and coordinated physiological process, and the different stages of this process have corresponding microenvironments to support cell development and physiological activities. However, biological scaffolds that provide different three-dimensional environments during different stages of bone regeneration are lacking. In this study, we report a novel composite scaffold (NPE@DCBM) inspired by the stages of bone regeneration; this scaffold was composed of a fibrin hydrogel loaded with nanoplatelet vesicles (NPVs), designated as NPE, and decellularized cancellous bone matrix (DCBM) microparticles. Initially, the NPE rapidly established a temporary microenvironment conducive to cell migration and angiogenesis. Subsequently, the DCBM simulated the molecular structure of bone and promoted new bone formation. *In vitro*, the NPVs regulated lipid metabolism in bone marrow mesenchymal stem cells (BMSCs), reprogramed the fate of BMSCs by activating the PI3K/AKT and MAPK/ERK positive feedback pathways, and increased BMSC functions, including proliferation, migration and proangiogenic potential. *In vivo*, NPV@DCBM accelerated bone tissue regeneration and repair. Initially, the NPE rapidly induced angiogenesis between DCBM microparticles, and subsequently, BMSCs differentiated into osteoblasts with DCBM microparticles at their core. In summary, the design of this composite scaffold that sequentially mimics different bone regeneration microenvironments may provide a promising strategy for bone regeneration, with clinical translational potential.

1. Introduction

Severe bone defects caused by high-energy trauma, such as fractures, cannot be resolved by self-repair, which seriously affects the quality of life of patients and is a major clinical challenge. Approximately 2.2 million patients worldwide undergo bone tissue transplantation each year [1]. At present, autologous bone transplantation remains the most effective method for bone regeneration, but it has potential risks, such as infection, nerve damage, and chronic pain at the donor site [2]. Other materials widely used in the clinic, such as polyetheretherketone (PEEK) and titanium alloys, show good biocompatibility, but their non-degradation ability and limited bone integration ability can easily lead

Peer review under the responsibility of editorial board of Bioactive Materials.
* Corresponding author. Department of Orthopaedic Surgery, The Third Hospital of Hebei Medical University, Shijiazhuang, 050051, China.
** Corresponding author.
*** Corresponding author. Department of Orthopaedic Surgery, The Third Hospital of Hebei Medical University, Shijiazhuang, 050051, China.
E-mail addresses: wangfeng5015@163.com (F. Wang), haofeng@decell.cn (F. Hao), wanglinfenglaoshi@163.com (L. Wang).
[1] Wenshuai Li, Qichen Shen and Tong Tong contributed equally to this work.

https://doi.org/10.1016/j.bioactmat.2025.04.018
Received 12 October 2024; Received in revised form 27 March 2025; Accepted 16 April 2025

to implant failure [3,4]. Therefore, the increased demand for bone grafts is driving the rapid development of the field of bone tissue engineering. For example, hydroxyapatite (HAP), bioactive glass (BS), sodium alginate (ALG), gelatin methacrylate (GelMa) and other composite scaffolds have shown good bone inductivity and bone conductivity in the context of bone repair [4–8], but their composition is different from that of natural bone tissue and cannot provide a suitable three-dimensional environment for bone tissue repair. Further research is needed to develop scaffolds with excellent bone repair ability.

The extracellular matrix (ECM) provides a three-dimensional microenvironment that is important for cell development and physiological activities. The biomimetic scaffolds used for tissue regeneration engineering should fully simulate this microenvironment to guide cell proliferation and differentiation [9,10]. Decellularized ECM (dECM) is one of the best natural candidates for simulating the complex properties of the ECM [11,12]. dECM from specific regions, tissues, or organs can guide stem cells to differentiate into their corresponding primitive lineage phenotypes [13–15]. dECM has been prepared from bone (decellularized bone matrix (DBM)), cartilage, fat, lung tissue and spleen tissue, and DBM has the greatest osteogenic ability [16]. In addition, our previous study revealed that compared with traditional DBM, decellularized cancellous bone matrix (DCBM), which is prepared via partial demineralization of cancellous bone, can increase stiffness and further promote osteogenic differentiation and bone repair [17]. However, bone regeneration is a complex and highly coordinated physiological process. Initially, fibrinogen is activated by thrombin to form a gel-like clot [18]. This spontaneously formed natural ECM with good viscoelasticity fills the site of injury and forms a hematoma. Hematomas are rich in bioactive factors (such as growth factors and inflammatory factors), which can rapidly establish a temporary microenvironment conducive to cell migration and angiogenesis [19–21]. Studies have shown that hematoma removal can lead to a significant delay in bone healing [22]. However, for critical-size bone defects, the characteristics of the hematoma change, which causes difficulties related to stem cell recruitment [23] and an excessive inflammatory response [24], thus affecting the bone regeneration process. Therefore, biomaterials that promote critical-size bone defect repair should not only account for tissue specificity to create a microenvironment conducive to osteogenesis but also simulate the dynamic process of tissue repair in the temporal dimension. Reconstruction of the hematoma stage is also essential for promoting bone regeneration. Although DCBM has been widely used in bone regeneration because of its excellent bone inductivity and bone conductivity, it still lacks the ability to simulate the bone regeneration microenvironment in the early stage to promote rapid stem cell migration and vascularization.

Platelets (PLTs) are anucleate blood cells that are produced via the lysis of mature megakaryocytes and contain secretory organelles that release factors such as coagulation factors, growth factors, adhesion molecules, and inflammatory factors [25,26]. PLTs play a central role in hematoma formation and the initial stage of tissue regeneration [27]. Many studies have reported that PLTs can be used as adjuvants to enhance the therapeutic effects of mesenchymal stem cells (MSCs) by promoting MSC migration, proliferation and angiogenesis potential [28–30]. PLTs can promote the proliferation and proangiogenic potential of MSCs by releasing growth factors that bind to target cell receptors or delivering bioactive mitochondria directly to the cytoplasm of target cells. In addition, PLTs and their products play important roles in bone repair [31,32]. However, PLTs are easily activated by various conditions (such as temperature, vibration, and pollution) during storage and transport, and the release of inflammatory factors by PLTs can lead to a stronger inflammatory response [33,34], which may hinder the bone healing process (especially for critical-size bone defects with intense inflammatory responses [24]). Nanomaterials are synthetic or natural materials that are smaller than 100 nm in any direction and have been reported to have better cellular functions than macroscale materials [1,35]. Nanoscale materials can simulate the pathways of bone cell differentiation and migration, and provide the required environment for the proliferation of various cells at the regenerative site [1]. Nanoplatelet vesicles (NPVs) are nanovesicles obtained by physical extrusion that exert PLT-like effects while preventing excessive release of inflammatory factors (possibly due to α-granule deficiency) [36,37]. We previously showed that NPV-based gels have the ability to limit excessive inflammation, promote angiogenesis and cell migration, and accelerate the repair of degenerative discs and wounds [37,38]. Therefore, we speculate that NPV-based materials can accelerate the healing of critical bone defects via microenvironmental regulation during the early stage of bone repair.

In this study, we developed a bone repair strategy that could sequentially mimic different bone regeneration microenvironments. To conduct this proof-of-concept study, we first explored the effects of NPVs on bone marrow mesenchymal stem cells (BMSCs), which are closely related to bone regeneration. The NPVs could reshape the fate of BMSCs and increase their proliferation, migration and proangiogenic potential. In terms of mechanism, the NPVs enhance lysophosphatidic acid (LPA) synthesis by reprogramming intracellular lipid metabolism, providing positive feedback to activate the PI3K/AKT and MAPK/ERK pathways, which are closely related to the fate of BMSCs (Scheme 1A). In addition, we reported on the use of a novel composite scaffold with sequential biomimetic ability (NPE@DCBM), which was composed of DCBM microparticles and a fibrin hydrogel loaded with the NPVs (NPE) (Scheme 1B). During the early stage of repair, the NPE established a temporary microenvironment similar to the hematoma microenvironment, and its soft and porous nature facilitated the migration and proliferation of BMSCs into the interior of the material and the rapid formation of blood vessels between DCBM microparticles. During the later stage of repair, after the degradation of the NPE, relatively dense and hard DCBM microparticles formed the osteoblast core at the regeneration site, and BMSCs differentiated into osteoblasts around the DCBM microparticles. Finally, we confirmed the bone regeneration ability of the NPE@DCBM by establishing a subcutaneous ectopic osteogenesis mouse model and a rat skull critical-size defect model.

2. Materials and animals

The CCK-8 assay kit, the EdU-488 cell proliferation assay kit, the BCA kit, calcein, DiI, and DiO were purchased from Beyotime Biotechnology (Shanghai, China). The IL-1β human ELISA kit (BMS224-2) and IL-6 human ELISA kit (BMS213-2) were purchased from Thermo Fisher Scientific (USA). The following primary antibodies used for Western blotting were from Proteintech (Beijing, China): anti-CD41 (24552-1-AP), anti-CD42 (12860-1-AP), anti-β-actin (20536-1-AP), and anti-GAPDH (10494-1-AP) antibodies. The following primary antibodies used for Western blotting were obtained from Cell Signaling Technology (Boston, USA): anti-PI3 kinase p85 (# 4292), anti-phospho-PI3 kinase p8 (# 17366), anti-Akt (# 4691), anti-phospho-Akt (# 4060), anti-p44/42 MAPK (Erk1/2) (# 4695), and anti-phospho-p44/42 MAPK (Erk1) (# 5726) antibodies. The anti-cytoplasmic phospholipase A2 antibody (ab307889) used for Western blotting was purchased from Abcam (Cambridge, USA). The primary antibodies used for immunofluorescence staining were obtained from the following sources: anti-ARG1 (16001-1-AP), anti-CD45 (60287-1-lg), anti-CD90 (27178-1-AP), anti-CD31 (80530-1-RR), and anti-osteocalcin (23418-1-AP) antibodies were purchased from Proteintech (Beijing, China), and the anti-iNOS antibody (ab178945) was obtained from Abcam (Cambridge, USA). Fibrinogen was purchased from Sigma–Aldrich (USA). The lyophilizing thrombin powder was purchased from Yige Pharmaceutical (Hunan, China). Sulfo-Cy5.5-NHS was purchased from Lumiprobe (USA). Endothelial cell culture medium was purchased from ScienCell Research Laboratory (Shanghai, China).

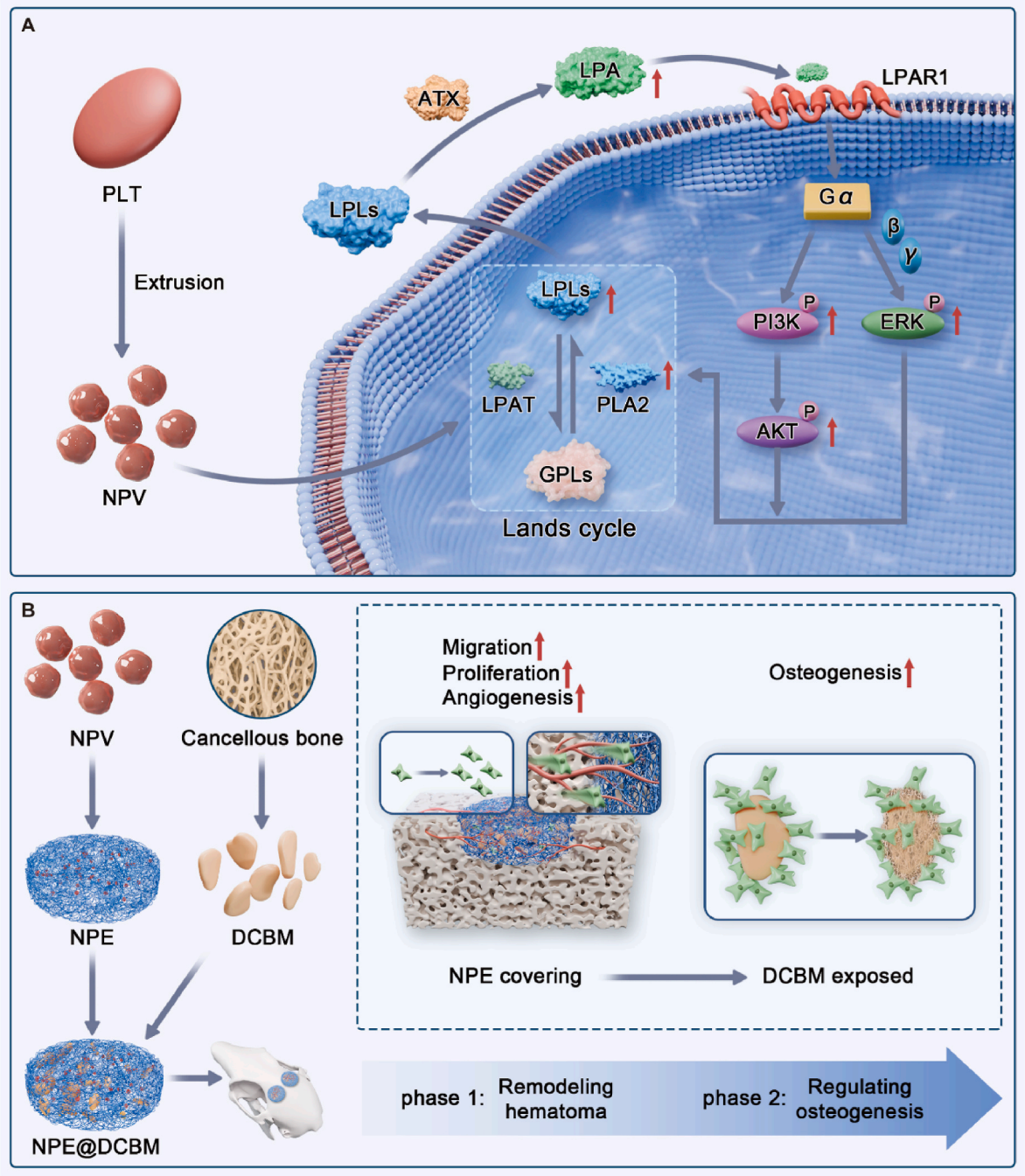

Scheme 1. Schematic diagram. (A) NPVs increase lysophosphatidic acid (LPA) synthesis by reprogramming intracellular lipid metabolism, providing positive feedback to activate the PI3K/AKT and MAPK/ERK pathways, which are closely related to BMSC fate, including proliferation, migration and angiogenic potential. (B) Functions of the composite scaffold with the ability to mimic sequential regeneration-specific microenvironments (NPE@DCBM): the NPE simulates the hematoma microenvironment during the early stage of injury and increases cell migration, proliferation and angiogenesis. During the later stage, after the degradation of NPE, DCBM particles constitute the osteogenic core, and BMSCs undergo osteogenic differentiation around the DCBM microparticles.

2.1. Preparation and characterization of the NPVs

PLTs were prepared via a previously described method [38] with slight modifications. All blood samples used in this study were approved by the Ethics Committee of the Third Hospital of Hebei Medical University, and informed consent was obtained (Ke 2024-072-1). In brief, whole blood from healthy donors was collected and mixed with citrate glucose solution A (ACD-A) anticoagulant (1 ml ACD-A/9 ml blood). After centrifugation at 100×g for 15 min, the supernatant was collected, and centrifugation was continued at 800×g for 20 min. The supernatant was discarded, and the sediment containing the PLTs was collected and stored for use after resuspension. To prepare the NPVs, the PLTs were first mixed with phosphate-buffered saline (PBS) containing ethylenediamine tetraacetic acid (EDTA, 5 mM, Sigma Aldrich) and prostaglandin e1 (PGE1, 1 mM, MCE) to prevent PLT activation. Next, the PLTs were passed through 1000 nm, 500 nm and 200 nm filters. Each step was repeated five times in a small extruder (Avanti Polar Lipids, AL, USA) with a polycarbonate membrane filter (Whatman, MA, USA). Finally, the sample was collected by centrifugation at 15000×g for 30 min to obtain the NPVs. The size and zeta potential of the samples were

measured via dynamic light scattering (DLS). The morphology and size of the samples were evaluated via cryo-transmission electron microscopy (cryo-TEM) (200 kV, FEI Tecnai G2 F20, USA). The particle sizes of the samples were measured via DLS at 0, 1, 3, 5 and 7 days to evaluate their stability. The protein concentration was measured with a BCA kit, and the protein components were characterized via Coomassie brilliant blue staining and Western blotting. To evaluate the ability of the NPVs to release inflammatory factors, ELISA kits were used to measure the levels of IL-1β and IL-6 in samples with or without thrombin. To evaluate the inflammatory response *in vivo*, we established a rat skull defect model and locally injected PLTs or NPVs (100 μg/mL). Seven days after injury, we performed immunofluorescence staining on the defect site to observe the fluorescence intensity of different macrophage types.

2.2. Cell culture

Human umbilical vein endothelial cells (HUVECs) were obtained from the China Center for Type Culture Collection (CCTCC). In accordance with previous studies [39], BMSCs were isolated and cultured from the bone marrow of the femurs and tibias of C57BL/6 mice. In brief, 4-week-old mice were killed, the femurs and tibias of the lower limbs were removed, the cells in the bone marrow cavity were rinsed with a 1 ml syringe, the cell suspension was then filtered through a 70 mm filter, any bone spurs or muscle and cell masses were removed, and the suspended cells were collected. The cells were cultured in DMEM supplemented with 10 % FBS (Gibco, USA) and 1 % penicillin–streptomycin (complete DMEM). After 3 h, the nonadherent cells were removed by replacing the medium. After another 8 h of culture, the medium was replaced again. Afterward, the medium was changed every 2 days. BMSCs at passages 4–6 were used for subsequent experiments.

2.3. NPV uptake assay

The uptake of NPVs by BMSCs was detected via confocal microscopy. To observe whether the NPVs were taken up by BMSCs, DiI fluorescent probes were incubated with the NPVs for 12 h, and the cells were washed with PBS three times to remove unbound probes. After the labeled NPVs were incubated with the BMSCs for 24 h, the nuclei were stained with two drops of Hoechst 33342 (Molecular Probes, Carlsbad, CA) for 15 min. The cells were then fixed with 4 % paraformaldehyde. Images were obtained via confocal fluorescence microscopy (Nikon, A1, Japan).

2.4. Effects of endocytosis inhibitors on NPV uptake

The pathway by which the NPVs were taken up by BMSCs was studied with different endocytosis inhibitors. The BMSCs were seeded in a 6-well plate and cultured until they reached 70–80 % confluency. Chlorpromazine (a clathrin-mediated endocytosis inhibitor), filipin III (a vesicle-mediated endocytosis inhibitor), wortmannin (a phosphatidylinositol 3-kinase-mediated microendocytosis inhibitor) and cytorelaxin D (an actin polymerization inhibitor) were added to the medium at concentrations of 50, 7.5, 5 and 5 μM, respectively. After 30 min of preincubation, the cells were treated with DiI-labeled NPVs (100 μg/ml) for 6 h in the presence of the inhibitor. Then, trypsinized cells were isolated via centrifugation and resuspended in PBS. Finally, the proportion of DiI-positive cells was quantitatively determined via flow cytometry.

2.5. Efficiency of NPV uptake by BMSCs

The efficiency of the uptake of NPVs and PLTs by BMSCs was compared via flow cytometry. First, the BMSCs were seeded in a 6-well plate and cultured until they reached 70–80 % confluency. The BMSCs were then treated with DiI-labeled NPVs or DiI-labeled PLTs for 6 h. The medium was removed, and the cells were washed with PBS, detached with trypsin, separated, rinsed 3 times with PBS, and immediately analyzed by flow cytometry to obtain the percentage of DiI-positive cells.

2.6. Cell viability assay

The viability of the BMSCs was determined with a CCK-8 kit. A total of 5×10^3 BMSCs were seeded into 96-well plates and pretreated with the PLTs or NPVs at different concentrations in complete DMEM for 24 h. To investigate cell viability at different times, the NPVs or PLTs were pretreated for 6, 12, 24, or 48 h. The medium was then replaced, and the BMSCs were cultured for 2 days. Finally, the medium was removed, and 100 μL of fresh medium supplemented with 10 μL of CCK-8 solution was added for 1 h at 37 °C. The OD was measured at 450 nm.

2.7. Cell counting analysis

BMSCs were inoculated in 24-well plates at a density of 1×10^4 cells/well. After pretreatment with 100 μg/mL PLTs or NPVs for 24 h, the BMSCs were cultured for 2 days. The medium was subsequently removed, and the mixture was subjected to trypsin digestion, centrifuged, and then resuspended in 1 ml of fresh medium. The final cell count was determined with a Countstar® Automatic Cell Counter (Shanghai, China).

2.8. EdU proliferation assay

BMSCs were inoculated in a confocal dish at a density of 1.5×10^5 cells/well and pretreated with the PLTs or NPVs for 24 h. The cells were then incubated with EdU (10 μM) for 4 h and fixed with 4 % paraformaldehyde for 20 min. The cells were permeabilized with 0.3 % Triton X-100 for 15 min, and the Click reaction mixture was added and incubated for 30 min at room temperature in the dark. Subsequently, nuclear staining was performed with Hoechst 33342. Finally, the incorporation rate of EdU was determined via confocal fluorescence microscopy (Nikon, A1, Japan).

2.9. Evaluation of BMSC migration

A scratch wound healing assay was used to evaluate the migration ability of the BMSCs. BMSCs were seeded in a six-well plate at a density of 2×10^5 BMSCs/well and cultured until they reached 70–80 % confluency. Then, the BMSCs were pretreated with the PLTs or NPVs (100 μg/mL) for 6 h. The medium was subsequently replaced, and linear scratches were made in the cell monolayer in the 6-well plate. The BMSCs were photographed at 0 and 24 h after injury. The migration ratio was measured with ImageJ software.

2.10. Evaluation of the angiogenic potential of BMSCs

The proangiogenic potential of the BMSCs was evaluated with a 6-well Transwell insert with an 8 μm pore size filter. Briefly, HUVECs were cultured until they reached 70–80 % confluency in the lower cavity, scratched with a sterile pipette tip and washed with PBS to remove unattached cells. BMSCs pretreated with the PLTs or NPVs (100 μg/mL) were then inoculated into the upper cavity at a density of 2×10^4 BMSCs/well. The HUVECs were photographed at 0 and 24 h after injury. The migration ratio was measured with ImageJ software. A tube formation assay was also used to evaluate the proangiogenic potential of the BMSCs. After the BMSCs were pretreated with the PLTs or NPVs (100 μg/mL) for 24 h, the medium was replaced, the cells were cultured for 2 days, and the supernatant was collected. Matrigel (Corning, USA) was added to 96-well plates at 50 μl per well and incubated at 37 °C for 1 h for gelation. Then, HUVECs were resuspended in the supernatant obtained above, inoculated into plates at a density of 2×10^4 BMSCs/well and incubated at 37 °C for 6 h. Tube formation was quantitatively

analyzed with ImageJ software.

2.11. Transcriptome sequencing

BMSCs were seeded in a six-well plate at a density of 2×10^5 BMSCs/well and incubated with or without the NPVs (100 μg/mL) for 24 h. The sequencing libraries were constructed with the NEBNext® Ultra™ RNA Library Prep Kit for Illumina® (#E7530L, NEB, USA) as recommended by the manufacturer. In brief, mRNA was purified from total RNA with poly-T oligo-attached magnetic beads. The first-strand cDNA was synthesized with a random hexamer primer and RNase H, and the second-strand cDNA was synthesized with buffer, dNTPs, RNase H and DNA polymerase I. The library fragments were purified with a QiaQuick PCR kit and eluted with EB buffer, and then terminal repair, A-tail addition and adapter addition were performed. Then, PCR was performed, and the library was completed. The index-coded samples were clustered with the cBot cluster generation system with the HiSeq PE Cluster Kit v4-cBot-HS (Illumina). The libraries were subsequently sequenced on the Illumina platform, and 150 bp paired-end reads were generated. The reference genomes and annotations were downloaded from the ENSEMBL database (http://www.ensembl.org/index.html). Genes with P values < 0.05 and absolute log2-fold changes ≥ 1 were considered differentially expressed genes (DEGs).

2.12. Western blot analysis

Proteins were extracted from the BMSCs of the different groups via RIPA buffer (Beyotime, China) containing 1 % protease inhibitor (PMSF) and phosphatase inhibitor. A BCA protein concentration kit (Beyotime, China) was used to measure the extracted protein concentration. The proteins were electrophoresed via 10 % SDS–PAGE and transferred from the gel to a polyvinylidene difluoride (PVDF) membrane (Millipore, Shanghai, China). The PVDF membrane was blocked with 5 % nonfat milk for 1 h. Then, the membrane was washed with Tris-HCl-buffered saline containing 0.1 % Tween-20 (TBST) 3 times for 5 min each. The membrane was subsequently incubated with primary antibodies (anti-CD41, anti-CD42, anti-β-actin, anti-GAPDH, anti-PI3 kinase p85, anti-phospho-PI3 kinase p8, anti-Akt, anti-phospho-Akt, anti-Erk1/2, anti-phospho-Erk1 and anti-cytoplasmic phospholipase A2 antibodies) at 4 °C for 12 h. The membrane was subsequently incubated with the corresponding secondary antibodies (1:5000) (Beyotime, China) for 1 h at room temperature. The target bands were visualized via enhanced chemiluminescence (ECL) (Thermo Fisher Scientific, USA), and the quantity of antigen–antibody complexes was further analyzed with ImageJ software.

2.13. Metabolomic analysis

BMSCs were treated as described for transcriptome analysis. Then, 1×10^6 cells were collected from each group for subsequent analysis. The cells were incubated for 2 min in 1 mL of precooled extractant (80 % methanol aqueous solution). The mixture was frozen for 3 min in liquid nitrogen after incubation on ice for 5 min, vortexed for 2 min and circulated 3 times. The mixture was subsequently centrifuged at 12000 r min^{-1} at 4 °C for 10 min. Finally, 200 μL of the supernatant was removed, and the mixture was placed in the inner liner of the corresponding injection bottle for on-board analysis. An LC–ESI–MS/MS system was used to analyze the extracts. The analytical conditions were as described previously [37]. Metabolites with P-values <0.05 and absolute log2-fold changes ≥ 1 were identified as differentially abundant metabolites. The identified metabolites were annotated via the KEGG Compound database, and the annotated metabolites were then mapped to the KEGG Pathway database (http://www.kegg.jp/).

2.14. LPA measurement

BMSCs were inoculated into 6-well plates at a density of 2×10^5 BMSCs/well and cultured until they reached 70–80 % confluency. The BMSCs were then pretreated with serum-free medium containing the NPVs (100 μg/mL) for 24 h. The supernatant was collected, and the level of LPA was determined with an ELISA kit (Cloud-Clone Corp, China).

2.15. Real-time quantitative polymerase chain reaction (RT–qPCR)

Total RNA was extracted from the BMSCs with TRIzol reagent (Invitrogen) and an RNA purification kit (CW0581, Kangwei). MMLV reverse transcription reagent (Takara) was used for reverse transcription into cDNA. RT–qPCR was performed with a SYBR Master Mix qPCR kit (Takara). The primers used are listed in Table 1.

2.16. Preparation and characterization of the DCBM

DCBM microparticles were prepared in a manner similar to our previously reported method [17,40,41]. In brief, fresh pig cancellous bone was obtained from local slaughterhouses, and the surrounding soft tissue, bone marrow and cartilage were removed. The cancellous bone was then cut into 3 mm pieces and washed with running water for 1 h. The pieces were soaked in 0.6 % (v/v) peracetic acid for 1 h and transferred to a solution containing 1 % (v/v) Triton-X100 (Sigma) in a Forma Orbital Shaker (Thermo Fisher Scientific, USA) at 100 rpm at 4 °C for 24 h. The pieces were washed with sterilized water and stirred continuously for 1 h; this process was repeated twice. The pieces were infused into 1 % (w/v) SDS solution (Fdbio Science Biotech Co. Ltd., China) and incubated on a shaker at 100 rpm at 23 °C for 36 h. Then, the cancellous bone pieces were immersed in decalcified solution and demineralized at 4 °C for 4 h for partial decalcification with a DeCa rapid decalcifier (DX-1100; Pro-Cure Medical Technology Co., Ltd., China). After decalcification, the samples were cleaned with deionized water and then crushed after ventilation and drying. DCBM microparticles with a diameter <500 μm were screened via filtration, radiation sterilization, and sealing. Histological analysis was performed via hematoxylin and eosin (H&E) and DAPI staining, and the cancellous bone tissue was crushed into microparticles as large as the DCBM microparticles and used as a control. For DNA quantification, DNA was extracted with a Universal Genomic DNA Kit (CW Biotech, China), and its concentration was measured at 260 nm with a microplate spectrophotometer (Multiskan GO, Thermo Fisher Scientific, USA). The appearance of the DCBM microparticles was visualized by scanning electron

Table 1
Sequences of the primers used for RT–qPCR.

Gene (F: forward; R: reverse)	Primer Sequence
LPAR1-F	GCTTCTACAATGAGTCTATCGCC
LPAR1-R	TGATGAACACGCAAACAGTGAT
LPAR2-F	CTTCCTCATGTTCCATACTGGC
LPAR2-R	GGCTGTGTAGCTGTACCGC
LPAR3-F	CAAGCGCATGGACTTTTTCTAC
LPAR3-R	GAAATCCGCAGCAGCTAAGTT
LPAR4-F	CTTCTGCTTCCGCATGAAAATG
LPAR4-R	GCCAGTGGCGATTAAAGTTGTA
LPAR5-F	ACCTGGACATGATGTTTGCCA
LPAR5-R	GAGACCAGTCGCCAATACCA
LPAR6-F	TCTGTACGGGTGCATGTTCAG
LPAR6-R	TGCCAGGTTAATCATGTACGTTG
ALP-F	CCAACTCTTTTGTGCCAGAGA
ALP-R	GGCTACATTGGTGTTGAGCTTTT
Runx2-F	GACTGTGGTTACCGTCATGGC
Runx2-R	ACTTGGTTTTTCATAACAGCGGA
OPN-F	ATCTCACCATTCGGATGAGTCT
OPN-R	TGTAGGGACGATTGGAGTGAAA
OCN-F	CTGACCTCACAGATCCCAAGC
OCN-R	TGGTCTGATAGCTCGTCACAAG

microscopy (SEM), and the size of the microparticles was analyzed with ImageJ software.

2.17. Preparation and characterization of the NPE

One hundred micrograms of NPVs were added to 1 mL of PBS solution containing 10 mg of fibrinogen (Yeasen, China) to prepare an NPE Pregel. Then, 20 U of thrombin (Sigma, USA) was added to the Pregel and allowed to stand for 5 min to fully activate fibrinogen to form the NPE. For visualization of the NPVs in the NPE, we constructed larger-diameter NPVs by changing the aperture of the filter and then observed the DiI-labeled NPVs via confocal fluorescence microscopy (Nikon, A1, Japan).

2.18. Preparation and characterization of the NPE@DCBM

DCBM microparticles were added to the NPE Pregel until they reached the level of the liquid, and the NPE@DCBM was prepared by adding thrombin (20 U/ml). The three-dimensional microstructure of freeze-dried NPE@DCBM with different fibrin concentrations (5 mg, 10 mg, and 20 mg) was observed via SEM, and the porosity was analyzed via ImageJ software. The rheological properties of the NPE@DCBM were evaluated with a rotating rheometer (HAAKE MARS 60, Germany). Five hundred microliters of the NPE@DCBM were placed on a parallel plate (40 mm). Frequency sweep tests were performed between 0.1 and 10 Hz using constant strain (1 %) at 37 °C. The shear-thinning behavior was characterized by measuring the linear viscosity at shear rates ranging from 0.01 to 100 s^{-1} at 37 °C. Mechanical compression analysis was performed with a universal testing machine (Zwick, Germany). A cylindrical NPE@DCBM sample was placed on the platform and compressed at a rate of 1 mm/min. The compressive stress and maximum deformation were obtained from the compressive stress–strain curve. To determine the rate of fibrin degradation in the NPE@DCBM, IVIS spectroscopic imaging was used to confirm the fibrin content. First, fibrinogen was labeled with Sulfo-Cy5.5-NHS, and the NPE@DCBM was prepared according to the method described above. Subsequently, 400 μL of the NPE@DCBM was implanted under the skin of a nude mouse. After implantation, the fluorescence intensity of the scaffold was quantified with Living Image software on days 0, 1, 3, 5 and 7. Additionally, after the material was implanted in the rats for 28 days, histological analysis of the heart, liver, spleen, lung, and kidney was performed by H&E staining to assess whether the material caused systemic toxicity.

2.19. ALP staining in vitro

BMSCs were inoculated in the lower transwell chamber (Corning, USA) of a 12-well plate at a density of 1×10^4 cells/well. The NPE, DCBM microparticles, or NPE@DCBM were placed in the upper chamber. After 24 h, the medium was changed to osteogenic induction medium containing 10^{-8} M dexamethasone (Sigma–Aldrich, USA), 10 mM β-glycerol phosphate (Sigma–Aldrich, USA), and 50 mg/L ascorbic acid (Sigma–Aldrich, USA). After 7 days, the cells were fixed and incubated with the BCIP/NBT kit (CWBIO, China) for 10 min. An ALP assay kit (Beyotime, China) was used to quantify ALP. The OD was measured at 405 nm.

2.20. Alizarin red S (ARS) staining in vitro

BMSCs were inoculated in the lower transwell chamber (Corning, USA) of a 12-well plate at a density of 1×10^4 cells/well. The NPE, DCBM microparticles, or NPE@DCBM were placed in the upper chamber. After 24 h, the medium was changed to osteogenic induction medium. After 14 days, the cells were fixed and stained with 1 % ARS solution at RT (Beyotime, China). The stains were subsequently dissolved in 10 % cetylpyridinium chloride (Sigma–Aldrich, USA) for 30 min. The OD was subsequently measured at 562 nm.

2.21. Bone regeneration effect of the NPE@DCBM in vivo

A subcutaneous ectopic osteogenesis assay was used to evaluate bone regeneration [3,42,43]. All animals used in this study were approved by the Ethics Committee of the Third Hospital of Hebei Medical University (Z2024-208-2). In brief, 8-week-old nude mice were anesthetized via an intraperitoneal injection of 1 % pentobarbital sodium. After anesthesia, the procedure was performed under aseptic conditions. An approximately 1 cm longitudinal incision was made in the skin on both sides of the back to create subcutaneous pockets. Two hundred microliters of the NPE@DCBM was subsequently implanted with the DCBM as a control. In the DCBM group, DCBM microparticles were placed in normal saline. The mice were allowed to eat and drink freely after surgery. The mice were euthanized 4 or 8 weeks after surgery. Different scaffolds were scanned at 4 and 8 weeks via microcomputed tomography (micro-CT) (SkyScan1275Buker, Belgium). 3D reconstruction and quantitative analysis of the BV and BV/TV were performed with SkyScan software. The scaffold was subsequently placed in 14 % EDTA (Sigma–Aldrich, Germany), decalcified at 37 °C for 7 days, and then embedded in paraffin sections. H&E and Masson's trichrome (MT) staining were used for internal characterization. In addition, immunofluorescence staining was performed with CD31 (Proteintech, China) to observe angiogenesis within these scaffolds. ImageJ software was used for quantitative analysis.

2.22. Repair of skull critical-size defects

Eight-week-old Sprague–Dawley rats (250 ± 50 g) were randomly distributed into the control group, NPE group, DCBM group or NPE@DCBM group. After anesthesia, the skin on the head was disinfected, and a small incision was made to expose the skull. Circular bone defects with a diameter of 5 mm were generated on both sides of the skull [31,44,45] (Precision Tools Co., Ltd., China). Different materials (blank, NPE, DCBM and NPE@DCBM) were injected into the bone defect site. The skin incision was closed with 2–0 absorbable sutures. Penicillin was injected continuously for 7 days to prevent infection. At 4 and 8 weeks after transplantation, the animals were euthanized via CO_2 asphyxia and cervical dislocation. The skull was collected and fixed in 4 % paraformaldehyde for subsequent study. The collected skulls were scanned via micro-CT (SkyScan1275Buker, Belgium), and 3D reconstruction and quantitative analysis of BV/TV and BMD were performed with SkyScan software. The skull was subsequently placed in 14 % EDTA (Sigma–Aldrich, Germany), decalcified at 37 °C for 30 days, and then embedded in paraffin sections. The regeneration of new bone was observed via H&E and MT staining. In addition, immunofluorescence staining for CD31 (Proteintech, China) and osteocalcin (OCN) (Proteintech, China) was used to observe angiogenesis and osteogenesis at the site of injury, respectively. To evaluate the number and distribution of BMSCs at the injury site early, we followed the same modeling and grouping methods. However, 7 days postinjury, immunofluorescence staining for CD45 (Proteintech, China) and CD90 (Proteintech, China) was performed. ImageJ software was used for quantitative analysis.

2.23. Statistical analysis

All the statistical analyses were performed with GraphPad Prism 10.0 software. The results are expressed as the means ± standard deviations (SDs). Tukey's multiple comparisons test or Student's *t*-test was applied after ANOVA to assess the statistical significance of our experimental results. Differences were considered significant when the p value was <0.05.

3. Results

3.1. Preparation and characterization of the NPVs

As in our previous study [38], the NPVs were obtained by pressing PLTs through filters with different pore sizes (Fig. 1A); this process relies on the principle of self-assembly of lipid membranes into spherical structures, with encapsulation of surrounding materials into the cavities of the generated nanovesicles. The particle size of the NPVs was analyzed via DLS (Fig. 1B), and the surface zeta potential was measured. The surface zeta potential of the PLTs was −30.8, and the surface zeta potential of the NPVs was −8.1. (Fig. 1C). In addition, the nanostructure of the NPVs was characterized via cryo-TEM (Fig. 1D). Next, we incubated the PLTs and NPVs at 37 °C for 1, 3, 5, and 7 days and found that the size of the PLTs gradually decreased, whereas the size of the NPVs remained relatively stable (Fig. 1E).

In addition, we determined the protein composition of the PLTs and NPVs and found that their composition was slightly different via Coomassie Brilliant Blue staining (Fig. 1F). Membrane marker proteins (CD41 and CD42) were significantly enriched in the NPVs, whereas the levels of cytoplasmic proteins (GAPDH and β-actin) were lower in the NPVs (Fig. 1F). This is because during the pressing process, vesicles can randomly wrap around the surrounding cellular components, and some unpackaged proteins or components are lost [46]. Next, we evaluated the ability of PLTs and PEVs to produce inflammatory factors after activation. We found that the production of IL-1β and IL-6 in PLTs significantly increased after the addition of thrombin, whereas there was no significant change in the production of these factors in the NPVs (Fig. 1G). To further assess the biological impacts of the NPVs and PLTs on bone defect repair, *in vivo* experiments were conducted with a focus on inflammation at the defect sites. Compared with the PLT group, the NPV group presented reduced expression of iNOS, which is known to drive inflammatory responses, and increased expression of ARG1, which is associated with tissue repair processes (Fig. 1H-J). This may be attributed to the absence of α-granules (ranging in size from 200 to 300 nm) [36,47]. α-granules contain many inflammatory factors that are products of synthetic pathways that are rapidly triggered when PLTs are activated (a process known as mRNA signal-dependent translation), and many regenerative cytokines, such as transforming growth factor β (TGF-β) and platelet-derived growth factor (PDGF), are stored in precursor forms that can be rapidly released [48]. Considering that the diameter of a single protein is 3–6 nm [49], the NPVs can partially retain growth factors from PLTs and promote proliferation and angiogenesis after being absorbed by target cells.

3.2. Characterization of NPV uptake by BMSCs

Considering the important role of BMSCs in bone regeneration, we investigated NPV uptake by BMSCs. First, NPVs labeled with the DiI membrane probe were cocultured with BMSCs, and confocal microscopy indicated that the NPVs could be successfully taken up by the BMSCs (Fig. 1K). Next, we investigated the pathway by which the NPVs were taken up by cells by using endocytosis inhibitors. Chlorpromazine, filipin III, wortmannin, and cytochalasin D inhibit clathrin-mediated endocytosis, caveolae-mediated endocytosis, micropinocytosis, and actin-mediated endocytosis, respectively. Flow cytometry revealed that the percentages of DiI-positive cells were 73.1 %, 74.6 %, 75.7 %, 53.9 %, 43.6 %, and 1.13 % in the control, chlorpromazine, filipin III, wortmannin, cytochalasin D, and 4 °C groups, respectively (Fig. 1L). Therefore, the uptake of the NPVs by BMSCs was mediated mainly by actin-mediated endocytosis and micropinocytosis. In addition, we found that the NPVs were more easily taken up by BMSCs than were the PLTs (Fig. 1M).

3.3. NPVs stimulate the proliferation and migration of BMSCs

To evaluate whether the NPVs promote the proliferation potential of BMSCs, we treated BMSCs with different concentrations of NPVs and observed the activity of the BMSCs through the CCK8 assay. The results revealed that the NPVs promoted BMSC proliferation in a concentration-dependent manner, and the optimal concentration of NPVs was determined to be 100 μg/mL (Fig. 2A). In addition, when the treatment time of NPV is 24 h, it exhibits a good effect of promoting cell vitality. (Fig S1). Microscopy results revealed that the proliferation of the BMSCs in the NPV-treated group was greater than that in the PLT-treated group (Fig. 2B). Cell counting also revealed similar results (Fig. 2C). We also compared the proliferation of BMSCs in different groups via the incorporation of EdU and then determined the percentage of EdU-positive cells via confocal microscopy. The results revealed that the NPV-treated group had the highest proportion of EdU-positive cells (Fig. 2D and G). Given that the migration of BMSCs is crucial for tissue repair, we evaluated the effect of the NPVs on the migration of BMSCs through a scratch wound assay. The results showed that both the PLTs and NPVs promoted the migration of BMSCs and that the NPVs had the greatest effect (Fig. 2E and H). In summary, our results revealed that the NPVs stimulate the proliferation and migration of BMSCs and have better effects than the PLTs do, which may be attributed to the presence of fewer inflammatory factors in the NPVs and the fact that BMSCs take up NPVs more easily (Fig. 1G and M).

3.4. NPVs stimulate the proangiogenic potential of BMSCs

Owing to the proangiogenic potential of MSCs and the fact that PLTs can enhance this property [29], we investigated whether the NPVs can increase the proangiogenic potential of BMSCs. First, we treated BMSCs with NPVs and then cocultured the treated BMSCs with HUVECs. Through a scratch wound assay, we found that both the PLTs and NPVs promoted the migration of HUVECs, with the NPVs exhibiting the strongest effect (Fig. 2F and J). In addition, we evaluated the proangiogenic potential of BMSCs subjected to different treatments through HUVEC tube formation experiments. The formation of endothelial tubes was significantly greater in the NPV group than in the other groups (Fig. 2I and K).

3.5. NPVs promote the proliferation and proangiogenic potential of BMSCs through the PI3K/AK and MAPK/ERK pathways

To explore the potential mechanism by which the NPVs promote the proliferation and proangiogenic potential of BMSCs, we analyzed the unique RNA changes within cells after NPV treatment through RNA sequence analysis (RNA-Seq). Principal component analysis (PCA) revealed that the repeated sequences of the cells in the two treatment groups were tightly clustered, forming different and repeatable subgroups (Fig. 3A). In total, 4210 genes were upregulated in the NPV group, including some genes related to cell proliferation and angiogenesis, and 4075 genes were downregulated (absolute $\log_2$-fold change ≥ 1, $p < 0.05$) (Fig. 3B). The NPVs promoted the regeneration-related functions of BMSCs, such as cell proliferation, migration, and proangiogenic potential (Fig. 2). This finding was consistent with the results of our GO analysis, in which the DEGs were enriched mainly in cytokine activity, growth factor activity, positive regulation of angiogenesis, positive regulation of cell population proliferation and positive regulation of migration (Fig. 3C). In addition, we found that the NPVs regulated the inflammatory response and immune response of BMSCs, which may be due to residual inflammatory factors in the NPVs. During NPV production via extrusion, vesicles randomly encapsulate cellular components, which may contain some residual inflammatory factors. As previously noted, although the NPVs markedly decreased IL-6 and IL-1 production compared with PLTs, some residual inflammatory factors were still present (Fig. 1G).

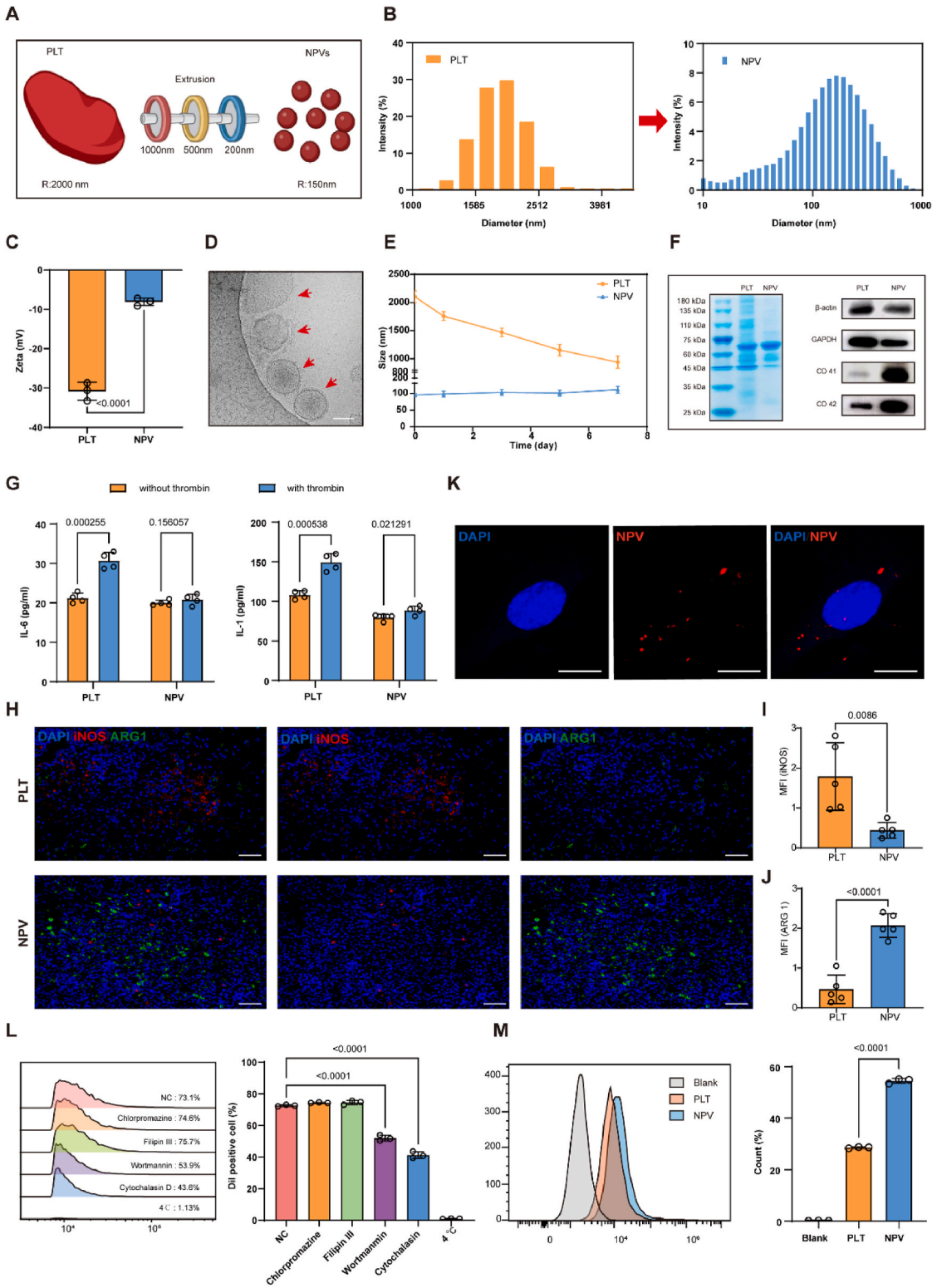

Fig. 1. Preparation and characterization of the nanoplatelet vesicles (NPVs). (A) Schematic diagram of NPV preparation. (B) Diameter of platelets (PLTs) and NPVs. (C) Zeta potential of PLTs and NPVs (n = 3). (D) Cryo-transmission electron microscopy (cryo-TEM) images of NPVs; scale bars = 100 nm. (E) Stability of PLTs and NPVs. (F) Coomassie brilliant blue staining and Western blot analysis of PLTs and NPVs. (G) Quantification of IL-1β and IL-6 from PLTs and NPVs with or without thrombin (n = 4). (H–J) Immunofluorescence staining (H) and quantification of the mean fluorescence intensity of iNOS (I) and ARG1 (J) before NPV treatment; scale bars = 50 μm (n = 5). (K) Fluorescence confocal microscopy image of NPV uptake; scale bars = 5 μm. (L) DiI-positive BMSCs were detected by flow cytometry after treatment with NPVs (labeled with DiI), and the proportion of DiI-positive BMSCs was quantified (n = 3). BMSCs were pretreated separately with different endocytosis-related inhibitors for 0.5 h. (M) DiI-positive BMSCs were detected by flow cytometry after treatment with NPVs or PLTs (labeled with DiI), and the proportion of DiI-positive BMSCs was quantified (n = 3). Differences were considered significant when the p value was <0.05.

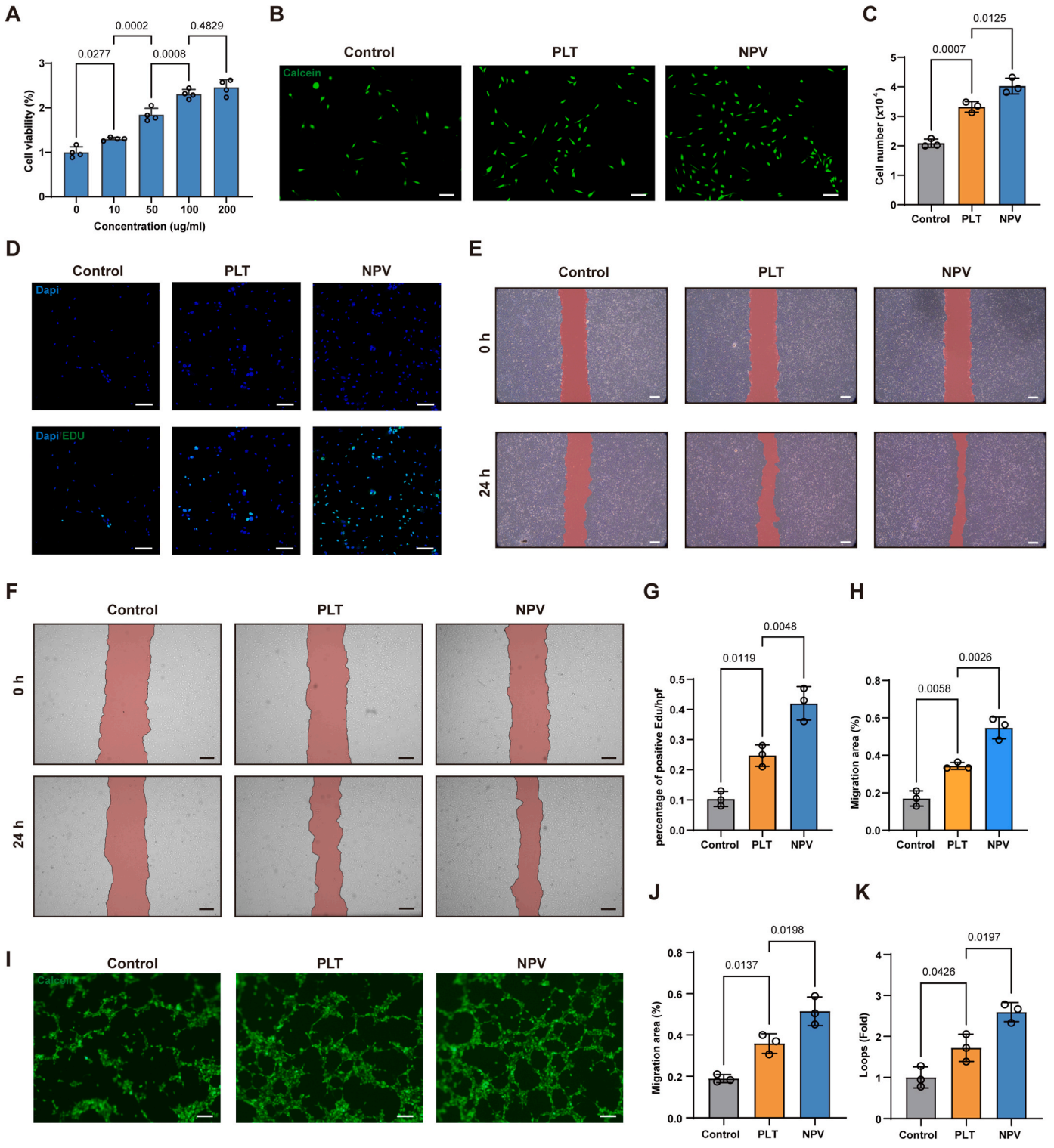

Fig. 2. NPVs increase the proliferation, migration and proangiogenic potential of BMSCs. (A) CCK-8 assay of BMSCs with different concentrations of NPVs (n = 4). (B) Representative images of BMSCs; scale bars = 100 μm. (C) Cell counts of the BMSCs (n = 3). (D and G) Representative images (D) and quantification (G) of the results of the EdU proliferation assay; scale bars = 100 μm (n = 3). (E and H) Representative images (E) and quantification (H) of BMSC migration; scale bars = 100 μm (n = 3). (F and J) Representative images (F) and quantification (J) of HUVEC migration; scale bars = 100 μm (n = 3). (I and K) Representative images (I) and quantification (K) of HUVEC tube formation; scale bars = 50 μm (n = 3). Differences were considered significant when the p value was <0.05.

A heatmap was generated to show the upregulation of regeneration-related genes after NPV treatment (Fig. 3D). GSEA also revealed that in NPV-treated BMSCs, components of pathways related to stem cell proliferation, sprouting angiogenesis, the regulation of cell migration involved in sprouting angiogenesis, and wound healing were significantly upregulated (Fig. 3E). In addition, KEGG pathway analysis was used to explore the potential mechanism by which the NPVs stimulate BMSCs. Cellular process analysis revealed that the NPVs regulated the pluripotency of stem cells, with enrichment of the PI3K/AKT and MAPK pathways (Fig. 3F). Previous studies have shown that the PI3K/

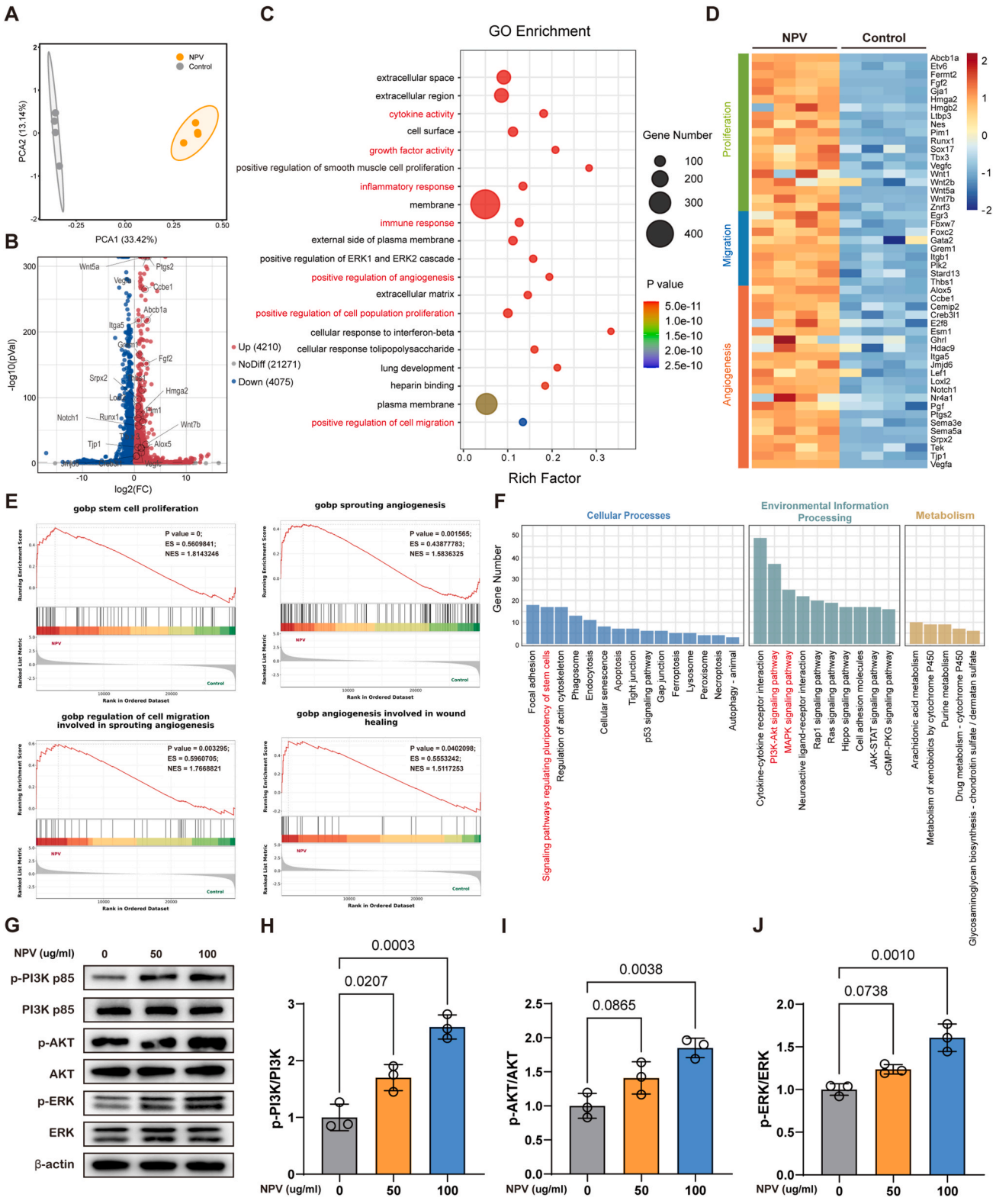

Fig. 3. NPVs increase the proliferation and proangiogenic potential of BMSCs through the PI3K/AK and MAPK/ERK pathways. (A) PCA of genes in BMSCs after treatment with NPVs. (B) Volcano plots showing differentially expressed genes in BMSCs. (C) Gene Ontology (GO) enrichment analysis of differentially expressed genes after treatment with NPVs. (D) Heatmap showing proliferation-, migration-, and angiogenesis-related genes after treatment with NPVs. (E) Gene set enrichment analysis (GSEA) was applied to compare the gene sets involved in cell proliferation, sprouting angiogenesis, the regulation of cell migration involved in sprouting angiogenesis, and wound healing. (F) Kyoto Encyclopedia of Genes and Genomes (KEGG) enrichment analysis of the pathways involved in the biological effects induced by NPVs. (G) Western blot analysis showing the phosphorylation levels of PI3K/AKT and ERK after treatment with NPVs. (H–J) Quantification of the results of the Western blot analysis (n = 3). Differences were considered significant when the p value was <0.05.

AKT and MAPK/ERK pathways are closely related to cell proliferation and angiogenesis [50–55]. Therefore, we further investigated by Western blotting whether the NPVs activate the PI3K/AKT and MAPK/ERK pathways. Consistent with the RNA-Seq results, the results of the Western blot analysis revealed a significant increase in the phosphorylation levels of PI3K/AKT and ERK (Fig. 3G-J). In summary, our results revealed that the NPVs stimulate the regeneration-related functions of BMSCs through the PI3K/AK and MAPK/ERK pathways.

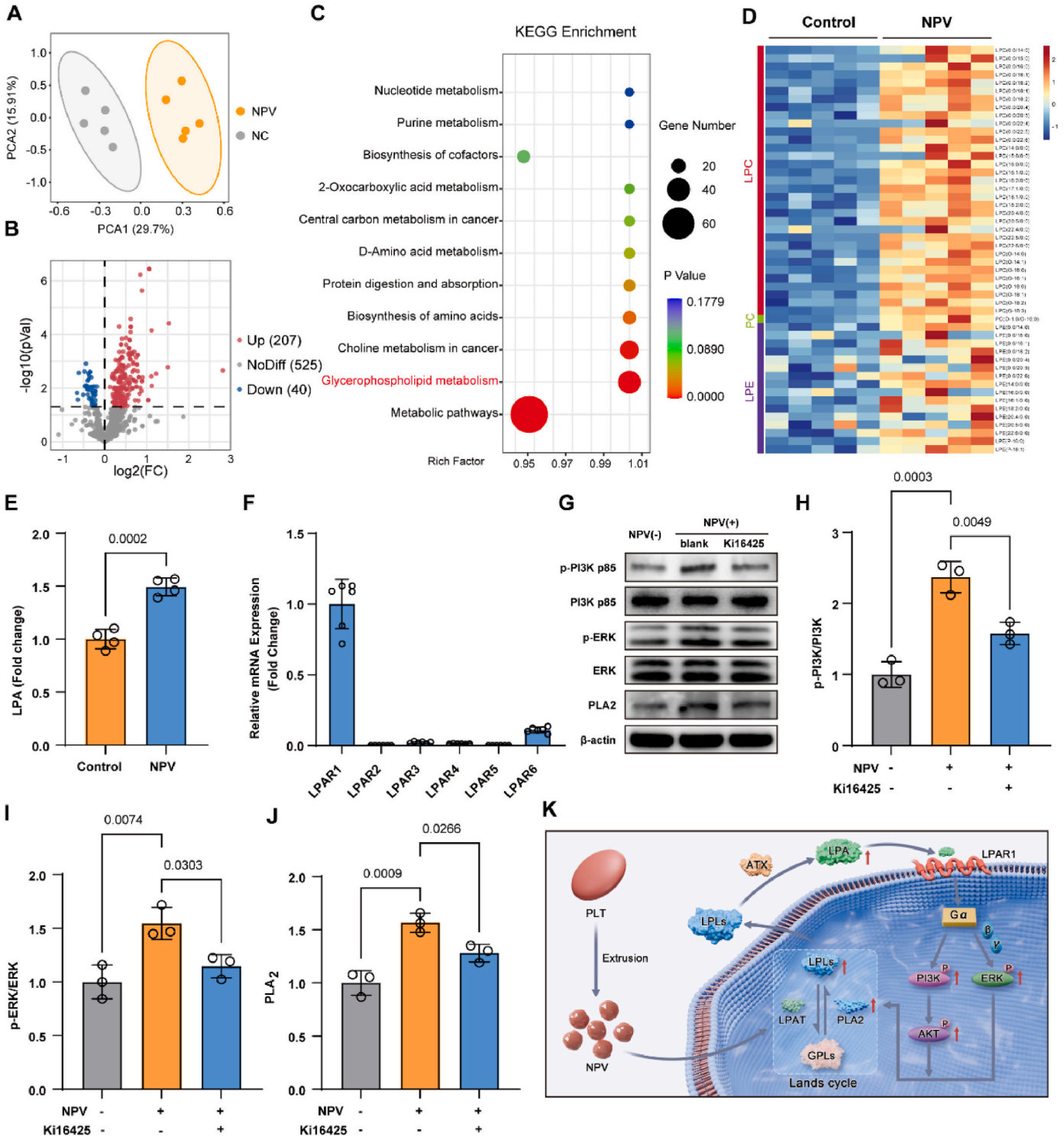

Fig. 4. NPVs induce lipid metabolism reprogramming in BMSCs to provide positive feedback for the PI3K/AKT and MAPK/ERK pathways. (A) PCA of metabolites in BMSCs after treatment with NPVs. (B) Volcano plots showing differentially abundant metabolites in BMSCs. (C) Kyoto Encyclopedia of Genes and Genomes (KEGG) enrichment analysis of the pathways involved in the biological effects induced by NPVs. (D) Heatmap showing lysophospholipid metabolites after treatment with NPVs. (E) Quantification of extracellular lysophosphatidic acid (LPA) with or without NPVs (n = 4). (F) Quantification of LPA receptor 1–6 (LPAR1-6) in BMSCs via RT−PCR. (G) Western blot analysis showing the phosphorylation levels of PI3K, ERK and PLA2 after treatment with the LPAR1/3 antagonist Ki16425. (H–J) Quantification of the results of the Western blot analysis (n = 3). (K) Schematic diagram of the process by which NPVs remodel BMSC lipid metabolism via positive feedback through the PI3K/AKT and MAPK/ERK pathways. Differences were considered significant when the p value was <0.05.

3.6. NPVs induce lipid metabolism reprogramming in BMSCs to provide positive feedback to the PI3K/AKT and MAPK/ERK pathways

To further investigate how the NPVs activate the PI3K/AKT and MAPK/ERK pathways, we conducted metabolomics analysis of NPV-treated BMSCs. PCA revealed that the metabolites present in the NPV group were different from those in the control group (Fig. 4A). A total of 772 metabolites were identified, and compared with the control group, the NPVs increased the abundance of 207 metabolites and decreased the abundance of 40 metabolites (absolute $\log_2$-fold change ≥ 1, $p < 0.05$) (Fig. 5B). Through KEGG analysis, it was found that metabolites with substantial differences in abundance were enriched in glycerophospholipid metabolism (Fig. 4C). We subsequently analyzed all the changes in glycerophospholipid metabolite levels and found that all the differentially abundant metabolites of the glycerophospholipids detected were mainly lysophospholipid metabolites (LPLs), such as lysophosphatidylcholine (LPC) and lysophosphatidylserine (LPE), in the BMSCs (Fig. 4D). The decomposition of intracellular glycerophospholipids (GPLs) into LPLs is catalyzed by phospholipase A2 (PLA2) [56]. LPLs can be rapidly converted into GPLs by lysophospholipid acyltransferases (LPATs) via the Lands cycle [56] or can be further converted into LPA, a multiacting lysophosphatidic mediator, by autotaxin (lysophospholipase D) [57]. GPLs are fundamental components of biofilms. We found that the NPVs retained most of the membrane components of PLTs and were more easily taken up by BMSCs than were PLTs (Fig. 1F and M). Therefore, the NPVs provided sufficient raw materials for lipid metabolism in BMSCs and promoted the generation of LPLs through the Lands cycle. LPA can regulate the proliferation and migration of stem cells and angiogenesis [58–61], and therefore, we measured the levels of extracellular LPA. Compared with the control treatment, the NPVs significantly increased the concentration of LPA (Fig. 4E). LPA acts by interacting with protein-coupled receptor family members (LPAR1-6) [62], and we found that only *LPAR1* was highly expressed in BMSCs (Fig. 4F). Subsequently, we found that the cell viability of NPV-treated BMSCs decreased significantly after treatment with Ki16425 (an LPAR1 and LPAR3 antagonist) [63] (Fig. S2). In addition, further investigations were conducted after adding Ki16425 to confirm whether the NPVs activate the PI3K/AKT and MAPK/ERK pathways via LPA. As expected, the phosphorylation of PI3K/AKT and ERK was significantly inhibited (Fig. 4G–I). The PI3K/AKT and MAPK/ERK pathways can increase the level of PLA2 to further increase the production of LPLs [64,65]. Therefore, we also investigated the level of PLA2 and found that the expression of PLA2 was reduced in the presence of Ki16425 (Fig. 4G and J). On the basis of these findings, we concluded that the NPVs regulate the lipid metabolism of BMSCs, activating the PI3K/AKT and MAPK/ERK positive feedback pathways via LPA (Fig. 4K).

3.7. Preparation and characterization of scaffolds with the ability to establish sequential regeneration-specific microenvironments

Our previous study revealed that DCBM has excellent bone inductivity and conductivity [17]. In this study, pig trabecular bone was used as the material to prepare the DCBM, allowing us to simulate a tissue-specific microenvironment that promotes osteogenesis. However, a crucial paradox of materials for regeneration is that for dense bone tissue, it is necessary for the material to have good mechanical properties while promoting cell migration to promote tissue function and repair. Therefore, we ground the DCBM into microparticles to increase the possibility of cell migration into the scaffold interior [66,67]. On the one hand, cells can enter the interior of the composite scaffold through the gap between dense DCBM microparticles, and in addition, the contact area between cells and DCBM microparticles is also increased. Representative sections stained with H&E and DAPI revealed that the DCBM successfully cleared cells, cell fragments, and nuclei (Fig. 5A and Fig. S3). DNA-identification analysis also revealed that only 6.43 ng of DNA remained in the DCBM sample per milligram of tissue (Fig. 5B). The appearance of the DCBM was subsequently evaluated by scanning electron microscopy (SEM), and the particle size was subjected to statistical analysis (Fig. 5C).

We introduced a fibrin hydrogel containing the NPVs (NPE) to simulate the ECM microenvironment during the early stage of tissue regeneration. On the one hand, fibrin is the most important extracellular matrix component during the early stage of injury, providing a temporary three-dimensional scaffold environment for early cell migration and angiogenesis [19–21]; on the other hand, the NPVs further increased the migration, proliferation, and proangiogenic potential of BMSCs (Fig. 2). To obtain the NPE in this study, the NPVs were added to a fibrinogen solution. After the addition of thrombin, the solution was converted into a gel similar to the NPE within a few min (Fig. 5D). The three-dimensional confocal fluorescence microscopy results revealed that the red fluorescence-labeled NPVs were evenly distributed throughout the hydrogel (Fig. 5E).

DCBM microparticles were added to the NPE Pregel solution, and a bionic composite scaffold (NPE@DCBM) was formed via the addition of thrombin (Fig. 5F). The surface of the scaffold was observed via SEM (Fig. 5G-I). The pores of a scaffold facilitate cell migration. Our results revealed that when the concentration of fibrinogen was 20 mg/ml, the number of pores in the NPE@DCBM was significantly reduced (Fig. 5G and H). Therefore, we chose a fibrinogen concentration of 10 mg/ml for subsequent experiments. We also observed DCBM microparticles at a higher magnification (Fig. 5I). We found that the surface of the DCBM microparticles was smooth. This may be because the NPE forms a new coating on the surface of the DCBM. This finding indicated that cells initially developed in the microenvironment provided by the NPE and did not come into contact with the DCBM. In addition, we found that the NPVs were equally distributed in the NPE portion of the NPE@DCBM (Fig. S4). We subsequently investigated the rheological properties of the NPE@DCBM. The NPE and NPE@DCBM both exhibited similar behavior, with G' greater than G'' throughout the entire frequency and time range, which was consistent with the solid-like behavior of the three-dimensional network in the cementitious system, indicating that the three-dimensional network in the cementitious system had good stability (Fig. 5J). In addition, the DCBM significantly increased the G' and G'' values of the NPE@DCBM. We also tested the viscosity of the NPE@DCBM and found that as the shear rate increased, the viscosity gradually decreased, indicating that the NPV@DCBM exhibited shear-thinning behavior (Fig. 5K). Compression tests of NPV@DCBM were then performed, and the results revealed that the DCBM significantly improved the mechanical properties of the NPE (Fig. 5L). Notably, the compressive modulus of the NPE@DCBM increased by dozens of times compared with that of the NPE (Fig. 5M). This may be because the mechanics of the composite scaffold are determined by the new network of interconnected hard DCBM microparticles rather than by the surrounding soft NPE [66]. Although the modulus of the NPE@DCBM was not enough to achieve complete cortical bone, the relatively smaller modulus was more beneficial for cell mechanotransduction and stem cell osteogenic differentiation [68]. Therefore, with the degradation of the NPE, the NPE@DCBM was more conducive to creating a three-dimensional environment that promoted bone formation.

Finally, we labeled fibrinogen with Sulfo-Cy5.5-NHS and observed the degradation of fibrinogen in the composite scaffold in nude mice through fluorescence imaging with an *in vivo* imaging system (IVIS) (Fig. 5O). The results revealed that fibrin was rapidly degraded within one week (Fig. 5N). This indicated that the NPE mainly played a role during the early stages of regeneration, and as it degraded, the exposed DCBM guided the differentiation of cells in that region. In addition, we evaluated whether the material causes systemic toxicity, and the results revealed there was no significant damage to the heart, liver, spleen, lung, or kidney after 28 days of implantation (Fig. S5).

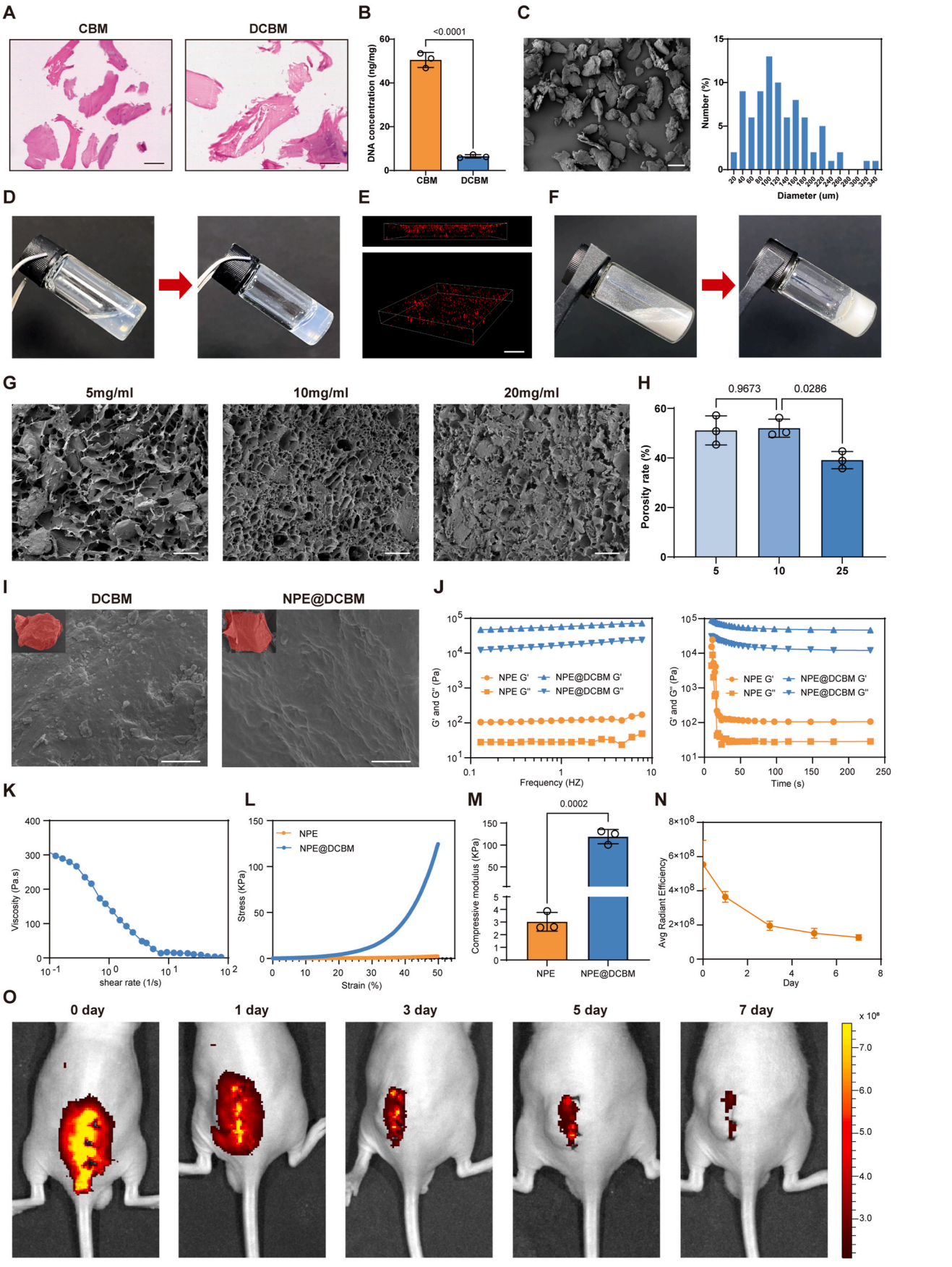

(caption on next page)

Fig. 5. Preparation and characterization of the NPE@DCBM. (A) H&E staining of cancellous bone matrix (CBM) and decellularized cancellous bone matrix (DCBM); scale bars = 100 μm. (B) Quantification of DNA before and after decellularization. (C) Representative images and quantification of the size of DCBM microparticles by scanning electron microscopy (SEM); scale bar = 200 μm. (D) *In vitro* gelation of the NPV fibrin hydrogel (NPE). (E) Representative images of the distribution of NPVs in the NPE; scale bars = 50 μm. (F) *In vitro* gelation of the NPE@DCBM. (G) SEM images of the structure of the NPE@DCBM with different fibrinogen concentrations; scale bars = 100 μm. (H) Porosity of the NPE@DCBM with different fibrinogen concentrations (n = 3). (I) Representative images of the DCBM surface modified by the NPE; scale bars = 5 μm. (J and K) Rheological properties of the NPE@DCBM: dynamic modulus (J) and viscosity (K). (L and M) The mechanical properties of the NPE@DCBM: compression stress−strain curves (L) and compressive modulus (M) (n = 3). (N and O) Representative images (O) and quantification (N) of the rate of fibrin degradation in the NPE@DCBM by IVIS spectroscopic imaging (n = 3). Differences were considered significant when the p value was <0.05.

3.8. *In vitro and in vivo bone regeneration effects of the NPE@DCBM*

First, the osteogenic effect of the NPE@DCBM on BMSCs was verified *in vitro*. BMSCs were incubated in osteogenic induction medium with different materials, in which the NPE@DCBM had a significant osteogenic effect (Fig. S6). Both ALP staining (Fig. S6A and S6B) and ARS staining (Fig. S6C and S6D) revealed increased osteogenic differentiation stimulated by the NPE@DCBM *in vitro*. In the NPE group, ALP increased, but bone mineralization was not significantly increased. This may be because the NPE mainly promotes the proliferation of BMSCs but does not promote their differentiation. Moreover, RT−qPCR detection of osteogenic genes revealed that the DCBM promoted osteogenesis, whereas NPE alone had no significant effect (Fig. S6E).

To further evaluate the osteogenic effects of the NPE@DCBM *in vivo*, subcutaneous ectopic osteogenesis experiments were conducted via the subcutaneous implantation of different scaffolds in nude mice (Fig. 6A). After 4 and 8 weeks, different implanted scaffolds maintained their size and shape, but the NPE@DCBM scaffolds formed bone-like tissue with a redder appearance, indicating that there may have been more vascularization (Fig. 6B). Micro-CT 3D reconstruction images of the separated scaffold tissue revealed that at 4 and 8 weeks after surgery, there was more new bone formation in the NPV@DCBM group than in the DCBM group, whereas there was less new bone formation in the DCBM group (Fig. 6C). Compared with those in the DCBM group, the new bone volume (BV) and the ratio of new bone volume to total volume (BV/TV) in the NPE@DCBM group were significantly greater (Fig. 6D and E). Sections stained with H&E and MT revealed increased angiogenesis between DCBM microparticles in the NPE@DCBM group at 4 and 8 weeks (Fig. 6F and G). In addition, immunofluorescence staining of the separated scaffold tissue for CD31 revealed a significant increase in the relative vessel area in the NPE@DCBM group (Fig. 6H and I).

3.9. *Repair of critical-size bone defects via NPE@DCBM*

To further validate the clinical potential of our new strategy, we established a skull critical-size defect model in rats and repaired the defects with NPVs, DCBM microparticles, and the NPE@DCBM. After 4 and 8 weeks of scaffold implantation, 3D reconstructions of horizontal and coronal micro-CT images were generated separately (Fig. 7A). The NPE@DCBM group showed a significant increase in bone regeneration, with more calcification and hard tissue formation in the skull defect area. Four weeks after surgery, compared with the other groups, the DCBM and NPE@DCBM groups presented significant increases in new bone formation. After 8 weeks, a large amount of new bone formation was observed in the defect area in the NPV, DCBM, and NPE@DCBM groups, but the NPE@DCBM group showed more significant penetration of regenerated bone tissue into the defect area (Fig. 7A). In addition, the NPE group promoted bone repair better than the control group did. This may be related to the role of the NPE in promoting angiogenesis and limiting excessive inflammatory responses [37,38]. Quantitative morphological analysis of regenerated bone via micro-CT images confirmed these results, with significant increases in bone mineral density (BMD) and regenerated bone volume (BV/TV, %) in the NPE@DCBM group compared with those in the other groups (Fig. 7B).

Histological observation revealed that the NPE@DCBM group had the best therapeutic effect after 4 weeks (Fig. 7C and D), which was consistent with the micro-CT results. The DCBM group and NPE@DCBM group had more organic bone matrix at the regeneration site. The NPE group and NPE@DCBM group presented more newly formed bone at the base of the regeneration site. To examine the distribution and quantity of BMSCs at the injury site early, CD45 and CD90 were used for labeling [69]. This experiment revealed that adding NPV markedly increased the number of BMSCs (CD45−/CD90+) at the injury site by day 7 (Fig S7). Semiquantitative immunofluorescence analysis of CD31 revealed that the NPE group and NPE@DCBM group presented greater neovascularization than the other groups did (Fig. 7E and F). In addition, to further verify whether the regeneration site undergoes osteogenesis with DCBM particles as the core, we conducted immunofluorescence labeling of OCN at this site. We found that the fluorescence intensity of the cells closer to the DCBM particles increased, and through the activity of the NPE, the osteogenic effect of the DCBM was further increased (Fig. 7G). Semiquantitative analysis further confirmed that the NPE@DCBM had the strongest osteogenic effect (Fig. 7H).

4. Discussion

In this study, we proposed a strategy of sequentially simulating a bone regeneration-specific environment for treating severe bone defects. First, cells involved in bone regeneration were rapidly recruited to the defect by constructing a temporary microenvironment similar to a hematoma. Then, upon the addition of the NPVs, the proliferation of BMSCs was enhanced, and the rapid formation of blood vessels was induced at the defect site. In the later stage of bone repair, with the degradation of the NPE, the DCBM formed a new osteogenic-specific microenvironment to promote osteogenic differentiation and accelerate the formation of new bone.

One of the most innovative points of the therapeutic strategy developed in this study was the introduction of an NPV-rich fibrin hydrogel into the scaffold. Notably, a clot with good viscoelasticity formed by fibrinogen activated by thrombin after tissue injury is not only specific to bone regeneration but also the key to initiating repair after any tissue injury in the body. Therefore, the introduction of the NPE into other tissue injury scenarios may also be applicable. In addition, the components of the NPE are human-derived, which fully reduces immune rejection between species and is more conducive to clinical translation.

PLTs are derived from megakaryocytes in the bone marrow [25,26]. Although the primary function of PLTs is to stop bleeding, they are involved in many physiological and regenerative processes, including cell proliferation, angiogenesis, wound healing, and bone regeneration [28–30,70]. PLTs are rich in many growth factors, immunoglobulins, and cytokines and actively participate in the process of tissue regeneration [71]. However, in some diseases, such as severe bone defects and diabetes-related skin lesions, excessive inflammation is an important factor in the failure of tissues to repair themselves [24,37]. With the rise of nanomedicine technology, PLT-based nanovesicles, including platelet-derived extracellular vesicles [72], platelet-derived apoptotic bodies [31], and nanoplatelet vesicles (NPVs) obtained directly by physical extrusion [38], have been extensively studied. The NPVs obtained directly by physical extrusion are simple to prepare and can reduce the release of inflammatory factors [37]. We conducted a series of previous studies on NPVs and found the following results: (1) NPVs have additional advantages in alleviating disc degeneration [38]; and (2) a natural extracellular matrix with NPVs and fibrin as the main

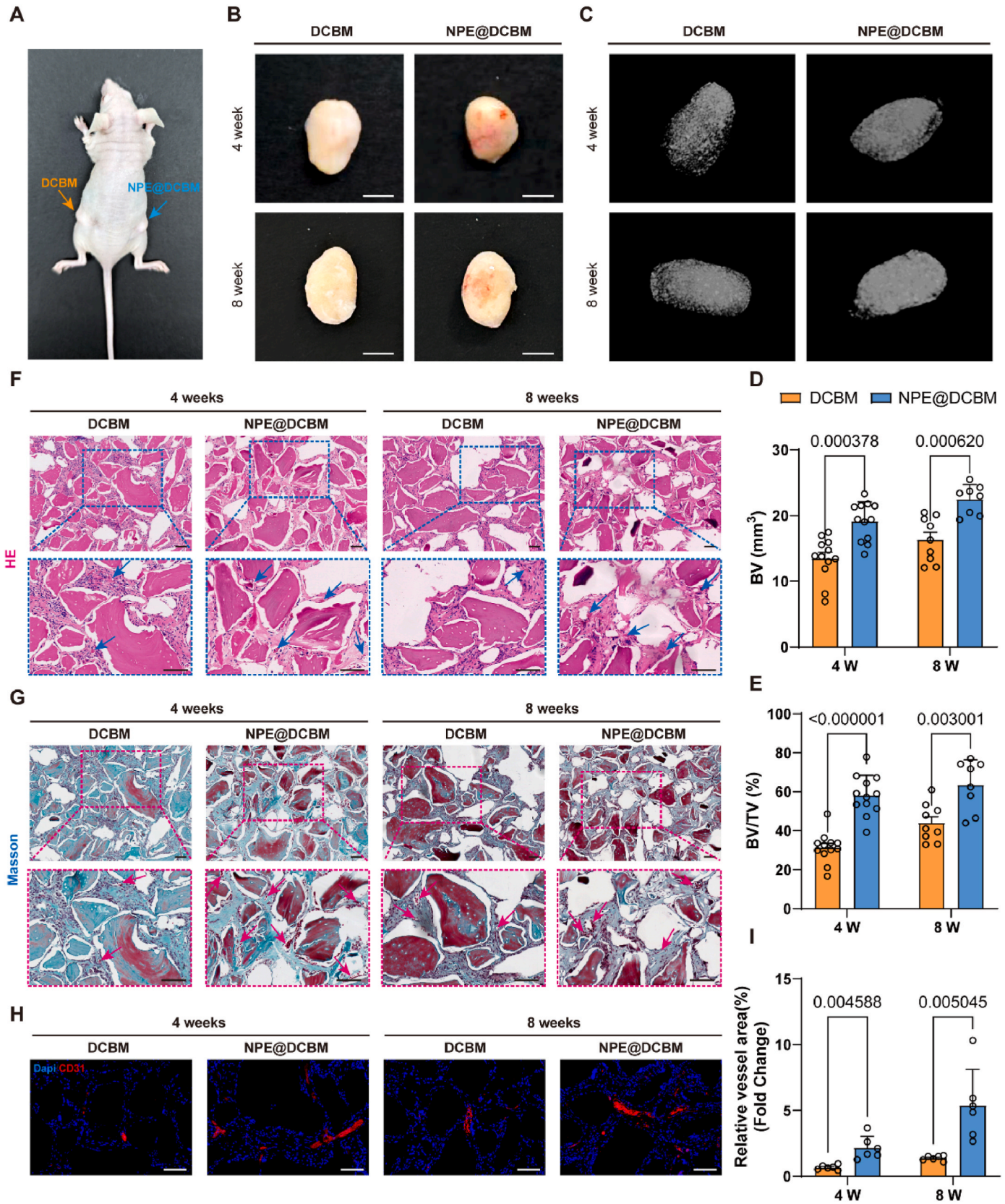

Fig. 6. *In vivo* bone regeneration effect of the NPE@DCBM. (A) Schematic diagram of the subcutaneous ectopic osteogenesis experiments. (B) General observation was performed after 4 and 8 weeks of implantation; scale bars = 5 mm. (C) 3D reconstructed micro-CT scanning images at 4 and 8 weeks after implantation. (D and E) Quantification of the volume of new bone (BV) and the bone volume/total volume (BV/TV) ratio (n > 6). (F) Representative images of the H&E-stained new bone structure; arrow: blood vessel; scale bars = 100 μm. (G) Representative images of the new bone structure after Masson's trichrome (MT) staining; arrow: blood vessel; scale bars = 100 μm. (H–I) Representative images (H) and quantification (I) of immunofluorescence staining for CD31 (red) in the new bone structure; scale bars = 100 μm (n = 6). Differences were considered significant when the p value was <0.05.

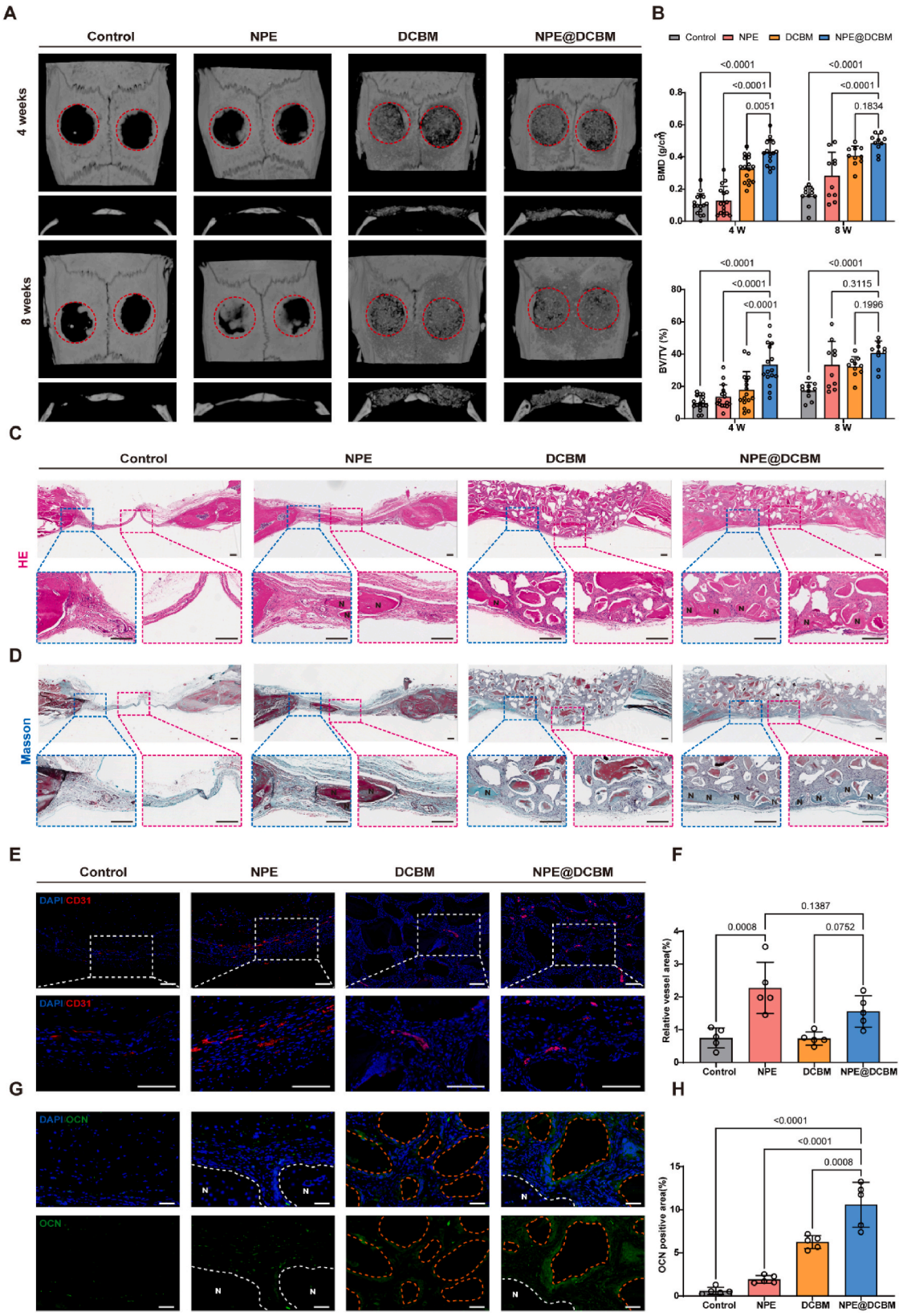

Fig. 7. Repair of critical-size bone defects with the NPE@DCBM. (A) 3D reconstructed micro-CT scanning images of skull defects and regenerated bone tissue. (B) Quantitative morphometric analysis of the bone mineral density (BMD) and bone volume/total volume (BV/TV) ratio of the skull defects via micro-CT analysis. (C) H&E staining of regenerated bone; N: new bone; scale bars = 200 μm. (D) Masson's trichrome (MT) staining of regenerated bone; N: new bone; scale bars = 200 μm. (E and F) Representative images (E) and quantification (F) of immunofluorescence staining for CD31 (red) in regenerated bone; scale bars = 100 μm (n = 5). (G and H) Representative images (G) and quantification (H) of immunofluorescence staining for OCN (green) in regenerated bone; N: new bone; orange dotted line: DCBM; scale bars = 50 μm (n = 5). Differences were considered significant when the p value was <0.05.

components can limit excessive inflammatory responses, accelerate angiogenesis, and promote diabetic wound healing [37]. In this study, we investigated the effect of NPVs on BMSCs for the first time. This study revealed that the NPVs were more easily taken up by BMSCs and had additional advantages in promoting BMSC functions, such as cell proliferation, migration, and angiogenesis. In addition, we explored the possible mechanisms by which the NPVs reprogrammed the fate of BMSCs. Through transcriptome sequencing, we found that the NPVs could activate the PI3K/AKT and MAPK-related pathways in BMSCs. Many studies have demonstrated that the PI3K/AKT and MAPK/ERK pathways regulate cell proliferation and angiogenesis [50–55]. The phosphorylation levels of PI3K/AKT and ERK were subsequently assessed and confirmed by *in vitro* experiments. The metabolic reprogramming of cells regulates their fate. To further verify how the NPVs activated this pathway, we found through metabolomics that the NPVs significantly changed the lipid metabolism level of BMSCs. The uptake of the NPVs by BMSCs increased the level of intracellular LPLs. The LPLs were subsequently transported outside the cell to transform into LPA through the activity of ATX. Studies have shown that LPA can regulate cell proliferation and differentiation by binding to receptors on the cell surface [58–61]. We found that LPA could activate the intracellular PI3K/AKT and MAPK-related pathways by acting on the LPAR1 receptor in BMSCs. In addition, the expression of PLA2, which is closely related to LPL synthesis, could be further improved. In summary, our study explored the important role of NPVs in BMSCs and elucidated their underlying mechanism.

Bone regeneration is a dynamic and carefully arranged physiological process. Ideally, a tissue-engineered bionic scaffold should fully simulate this dynamic three-dimensional microenvironment. The DCBM developed by partial demineralization has excellent biocompatibility, bone inductivity, and bone conductivity and is an ideal scaffold material for bone regeneration [17]. A key paradox of bone regeneration materials is the need to provide tissue-specific mechanical and biochemical properties while enabling cell migration to promote normal tissue function and repair. Previous studies have shown that dECM microparticles can increase the likelihood of cell migration to the interior of the scaffold [66,67]. In this study, to simulate the dynamic changes in the microenvironment at the regeneration site, we combined DCBM microparticles with the NPE to construct a composite biological scaffold that specifically mimics the bone regeneration microenvironment. Adding DCBM microparticles can significantly improve the mechanical properties of the scaffold, possibly because the stiffer DCBM microparticles form a new material skeleton. In addition, *in vivo* imaging experiments also revealed that the fibrin in the scaffold could be degraded *in vivo*. Both the subcutaneous ectopic osteogenesis mouse model and the rat skull critical-size defect model showed that the composite scaffold had good osteogenic effects. In addition, in animal experiments, the wide distribution of new blood vessels between DCBM microparticles and the growth of osteoblasts around DCBM microparticles as the core also demonstrated the angiogenic and osteogenic effects of different components in the scaffold.

This study provides a proof of concept that the bionic scaffold based on sequential simulation of different bone regeneration microenvironments achieved satisfactory therapeutic results, but it must be acknowledged that this study has some limitations. First, NPVs are mixtures loaded with a variety of biologically active molecules. Although our study revealed that the NPVs could activate the PI3K/AKT and MAPK pathways by remodeling lipid metabolism in BMSCs, the components of specific NPVs that play a major role have not yet been verified, and further studies are needed.

Second, we have demonstrated that the NPE@DCBM could promote angiogenesis and new bone formation, but other factors, such as the immune system, also play important roles in bone regeneration, which were not studied in great detail. In addition, the degradation rate of the NPE hydrogels within the first 3 days was relatively fast *in vivo*, possibly due to the body's plasminase system. However, further studies are needed to optimize its degradation rate. Finally, in addition to their use in the treatment of bone defects under normal physiological conditions, their application under other conditions, such as infection and cancers, needs further research.

5. Conclusion

In this study, we found that NPVs were more effective at promoting the proliferation, migration, and angiogenic potential of BMSCs than were PLTs. In terms of mechanism, the NPVs promoted the synthesis of extracellular LPA by remodeling lipid metabolism in BMSCs, with positive feedback activating the PI3K/AKT and MAPK/ERK pathways, which are related to proliferation and angiogenesis. Importantly, inspired by the process of bone regeneration, we constructed a composite scaffold that simulated the dynamic repair process of bone. The fibrin hydrogel simulated the three-dimensional bone repair environment during the hematoma stage and increased the regeneration-related functions of BMSCs via the loaded NPVs. The included DCBM microparticles significantly increased the scaffold strength while promoting osteogenic differentiation during the later stages of bone repair.

CRediT authorship contribution statement

Wenshuai Li: Writing – original draft, Investigation, Data curation. **Qichen Shen:** Writing – original draft, Investigation, Data curation. **Tong Tong:** Writing – original draft, Investigation, Data curation. **Hongsen Tian:** Investigation, Formal analysis. **Xiaowei Lian:** Visualization. **Haoli Wang:** Visualization. **Ke Yang:** Validation, Investigation. **Zhanqiu Dai:** Formal analysis. **Yijun Li:** Visualization. **Xianhua Chen:** Conceptualization. **Qingqing Wang:** Writing – review & editing. **Dan Yang:** Formal analysis. **Feng Wang:** Supervision, Methodology. **Feng Hao:** Writing – review & editing, Supervision. **Linfeng Wang:** Writing – review & editing, Funding acquisition, Conceptualization.

Ethics approval and consent to participate

All blood samples and animals used in this study were approved by the Ethics Committee of the Third Hospital of Hebei Medical University, and informed consent was obtained (Ke 2024-072-1 and Z2024-028-2).

Declaration of competing interest

Hao Feng, Yang Dan, and Shen Qichen are associated with companies that may have interests in the research outcomes. Hao Feng and Yang Dan are employed by Zhejiang DecellMatrix Biotechnology Co. Ltd., serving as Director of Research and Development and Chief Executive Officer (CEO), respectively. Shen Qichen is from Hangzhou OrigO Biotechnology Co. Ltd., working as a Research and Development Engineer. Their participation in this research is driven by scientific pursuits. However, they are committed to ensuring the objectivity and accuracy of the research, and have taken measures to avoid potential conflicts of interest.

The other authors, including Wenshuai Li, Tong Tong, Hongsen Tian, Xiaowei Lian, Haoli Wang, Ke Yang, Zhanqiu Dai, Yijun Li, Xianhua Chen, Qingqing Wang, Feng Wang, and Linfeng Wang, declare no competing interests related to this research. They have not received financial incentives that could influence the outcomes and contribute based on academic interests.

Collectively, all authors confirm that the research was conducted with integrity and adherence to ethical standards. They take responsibility for the accuracy and reliability of the findings and are committed to maintaining academic integrity throughout the research process and publication.

Acknowledgments

The study was supported by the central guidance for local scientific and technological development funding project (236Z7742G), the Hebei Natural Science Foundation (H2020206382) and Zhejiang Provincial Department of Science and Technology "Leading Geese" research and development project (Grant No. 2024C03072, 2023C03091 and 2022C03089). Ningbo Science and Technology Plan Project Key R&D Plan, "Unveiling the Leader" (2023Z194 and 2024Z211) and Hangzhou Key R&D Program (20231203A14), and Ningbo Science and Technology Plan Project (2024Z206).

Appendix ASupplementary data

Supplementary data to this article can be found online at https://doi.org/10.1016/j.bioactmat.2025.04.018.

References

[1] H. Yi, F. Ur Rehman, C. Zhao, B. Liu, N. He, Recent advances in nano scaffolds for bone repair, Bone Res. 4 (2016) 16050.
[2] D.S. Thoma, M. Payer, N. Jakse, S.P. Bienz, J. Hüsler, P.R. Schmidlin, U.W. Jung, C. H.F. Hämmerle, R.E. Jung, Randomized, controlled clinical two-centre study using xenogeneic block grafts loaded with recombinant human bone morphogenetic protein-2 or autogenous bone blocks for lateral ridge augmentation, J. Clin. Periodontol. 45 (2018) 265–276.
[3] Y. Wei, H. Pan, J. Yang, C. Zeng, W. Wan, S. Chen, Aligned cryogel fibers incorporated 3D printed scaffold effectively facilitates bone regeneration by enhancing cell recruitment and function, Sci. Adv. 10 (2024) eadk6722.
[4] P. Feng, P. Wu, C. Gao, Y. Yang, W. Guo, W. Yang, C. Shuai, A multimaterial scaffold with tunable properties: toward bone tissue repair, Adv. Sci. (Weinh.) 5 (2018) 1700817.
[5] Q. Li, H. Yu, F. Zhao, C. Cao, T. Wu, Y. Fan, Y. Ao, X. Hu, 3D printing of microenvironment-specific bioinspired and exosome-reinforced hydrogel scaffolds for efficient cartilage and subchondral bone regeneration, Adv. Sci. (Weinh.) 10 (2023) e2303650.
[6] L. Yang, L. Fan, X. Lin, Y. Yu, Y. Zhao, Pearl powder hybrid bioactive scaffolds from microfluidic 3D printing for bone regeneration, Adv. Sci. (Weinh.) 10 (2023) e2304190.
[7] C. Shuai, W. Yang, P. Feng, S. Peng, H. Pan, Accelerated degradation of HAP/PLLA bone scaffold by PGA blending facilitates bioactivity and osteoconductivity, Bioact. Mater. 6 (2021) 490–502.
[8] C. Shuai, X. Yuan, W. Yang, S. Peng, G. Qian, Z. Zhao, Synthesis of a mace-like cellulose nanocrystal@Ag nanosystem via in-situ growth for antibacterial activities of poly-L-lactide scaffold, Carbohydr. Polym. 262 (2021) 117937.
[9] L.E. Niklason, Understanding the extracellular matrix to enhance stem cell-based tissue regeneration, Cell Stem Cell 22 (2018) 302–305.
[10] Z. Sun, Z. Chen, M. Yin, X. Wu, B. Guo, X. Cheng, R. Quan, Y. Sun, Q. Zhang, Y. Fan, C. Jin, Y. Yin, X. Hou, W. Liu, M. Shu, X. Xue, Y. Shi, B. Chen, Z. Xiao, J. Dai, Y. Zhao, Harnessing developmental dynamics of spinal cord extracellular matrix improves regenerative potential of spinal cord organoids, Cell Stem Cell 31 (2024) 772–787.e11.
[11] X. Yang, Y. Ma, X. Wang, S. Yuan, F. Huo, G. Yi, J. Zhang, B. Yang, W. Tian, A 3D-bioprinted functional module based on decellularized extracellular matrix bioink for periodontal regeneration, Adv. Sci. (Weinh.) 10 (2023) e2205041.
[12] W. Liang, M. Han, G. Li, W. Dang, H. Wu, X. Meng, Y. Zhen, W. Lin, R. Ao, X. Hu, Y. An, Perfusable adipose decellularized extracellular matrix biological scaffold co-recellularized with adipose-derived stem cells and L6 promotes functional skeletal muscle regeneration following volumetric muscle loss, Biomaterials 307 (2024) 122529.
[13] G.M. Cunniffe, P.J. Díaz-Payno, E.J. Sheehy, S.E. Critchley, H.V. Almeida, P. Pitacco, S.F. Carroll, O.R. Mahon, A. Dunne, T.J. Levingstone, C.J. Moran, R. T. Brady, F.J. O'Brien, P.A.J. Brama, D.J. Kelly, Tissue-specific extracellular matrix scaffolds for the regeneration of spatially complex musculoskeletal tissues, Biomaterials 188 (2019) 63–73.
[14] Y. Jin, H. Kim, S. Min, Y.S. Choi, S.J. Seo, E. Jeong, S.K. Kim, H.A. Lee, S.H. Jo, J. H. Park, B.W. Park, W.S. Sim, J.J. Kim, K. Ban, Y.G. Kim, H.J. Park, S.W. Cho, Three-dimensional heart extracellular matrix enhances chemically induced direct cardiac reprogramming, Sci. Adv. 8 (2022) eabn5768.
[15] A.N. Cho, Y. Jin, Y. An, J. Kim, Y.S. Choi, J.S. Lee, J. Kim, W.Y. Choi, D.J. Koo, W. Yu, G.E. Chang, D.Y. Kim, S.H. Jo, J. Kim, S.Y. Kim, Y.G. Kim, J.Y. Kim, N. Choi, E. Cheong, Y.J. Kim, H.S. Je, H.C. Kang, S.W. Cho, Microfluidic device with brain extracellular matrix promotes structural and functional maturation of human brain organoids, Nat. Commun. 12 (2021) 4730.
[16] V. Beachley, G. Ma, C. Papadimitriou, M. Gibson, M. Corvelli, J. Elisseeff, Extracellular matrix particle-glycosaminoglycan composite hydrogels for regenerative medicine applications, J. Biomed. Mater. Res. 106 (2018) 147–159.
[17] S. Liu, Y. Wang, J. Wang, P. Qiu, S. Wang, Y. Shi, M. Li, P. Chen, X. Lin, X. Fang, A cancellous bone matrix system with specific mineralisation degrees for mesenchymal stem cell differentiation and bone regeneration, Biomater. Sci. 7 (2019) 2452–2467.
[18] J.M. Lord, M.J. Midwinter, Y.F. Chen, A. Belli, K. Brohi, E.J. Kovacs, L. Koenderman, P. Kubes, R.J. Lilford, The systemic immune response to trauma: an overview of pathophysiology and treatment, Lancet 384 (2014) 1455–1465.
[19] A. Elosegui-Artola, A. Gupta, A.J. Najibi, B.R. Seo, R. Garry, C.M. Tringides, I. de Lázaro, M. Darnell, W. Gu, Q. Zhou, D.A. Weitz, L. Mahadevan, D.J. Mooney, Matrix viscoelasticity controls spatiotemporal tissue organization, Nat. Mater. 22 (2023) 117–127.
[20] O.V. Kim, R.I. Litvinov, J.W. Weisel, M.S. Alber, Structural basis for the nonlinear mechanics of fibrin networks under compression, Biomaterials 35 (2014) 6739–6749.
[21] J. Ceccarelli, A.J. Putnam, Sculpting the blank slate: how fibrin's support of vascularization can inspire biomaterial design, Acta Biomater. 10 (2014) 1515–1523.
[22] X. Wang, T. Friis, V. Glatt, R. Crawford, Y. Xiao, Structural properties of fracture haematoma: current status and future clinical implications, J. Tissue Eng. Regen. Med. 11 (2017) 2864–2875.
[23] Y. Yang, Y. Xiao, Biomaterials regulating bone hematoma for osteogenesis, Adv. Healthcare Mater. 9 (2020) e2000726.
[24] P. Qiu, M. Li, K. Chen, B. Fang, P. Chen, Z. Tang, X. Lin, S. Fan, Periosteal matrix-derived hydrogel promotes bone repair through an early immune regulation coupled with enhanced angio- and osteogenesis, Biomaterials 227 (2020) 119552.
[25] T. Burnouf, H.A. Goubran, M.L. Chou, D. Devos, M. Radosevic, Platelet microparticles: detection and assessment of their paradoxical functional roles in disease and regenerative medicine, Blood Rev. 28 (2014) 155–166.
[26] C.W. Smith, Release of α-granule contents during platelet activation, Platelets 33 (2022) 491–502.
[27] M. Holinstat, Normal platelet function, Cancer Metastasis Rev. 36 (2017) 195–198.
[28] B. Hersant, M. Sid-Ahmed, L. Braud, M. Jourdan, Y. Baba-Amer, J.P. Meningaud, A. M. Rodriguez, Platelet-rich plasma improves the wound healing potential of mesenchymal stem cells through paracrine and metabolism alterations, Stem Cell. Int. (2019) 1234263, 2019.
[29] J. Levoux, A. Prola, P. Lafuste, M. Gervais, N. Chevallier, Z. Koumaiha, K. Kefi, L. Braud, A. Schmitt, A. Yacia, A. Schirmann, B. Hersant, M. Sid-Ahmed, S. Ben Larbi, K. Komrskova, J. Rohlena, F. Relaix, J. Neuzil, A.M. Rodriguez, Platelets facilitate the wound-healing capability of mesenchymal stem cells by mitochondrial transfer and metabolic reprogramming, Cell Metab. 33 (2021) 283–299.e9.
[30] M.R. Mahmoudian-Sani, F. Rafeei, R. Amini, M. Saidijam, The effect of mesenchymal stem cells combined with platelet-rich plasma on skin wound healing, J. Cosmet. Dermatol. 17 (2018) 650–659.
[31] Y. Jiang, Y. Zhu, Y. Shao, K. Yang, L. Zhu, Y. Liu, P. Zhang, X. Zhang, Y. Zhou, Platelet-derived apoptotic vesicles promote bone regeneration via golgi phosphoprotein 2 (GOLPH2)-AKT signaling Axis, ACS Nano 17 (2023) 25070–25090.
[32] Z. Badran, M.N. Abdallah, J. Torres, F. Tamimi, Platelet concentrates for bone regeneration: current evidence and future challenges, Platelets 29 (2018) 105–112.
[33] Y.Z. Xiang, Y. Xia, X.M. Gao, H.C. Shang, L.Y. Kang, B.L. Zhang, Platelet activation, and antiplatelet targets and agents: current and novel strategies, Drugs 68 (2008) 1647–1664.
[34] E. Anitua, M. Zalduendo, M. Troya, S. Padilla, G. Orive, Leukocyte inclusion within a platelet rich plasma-derived fibrin scaffold stimulates a more pro-inflammatory environment and alters fibrin properties, PLoS One 10 (2015) e0121713.
[35] A. García-García, S. Pigeot, I. Martin, Engineering of immunoinstructive extracellular matrices for enhanced osteoinductivity, Bioact. Mater. 24 (2023) 174–184.
[36] H. Jung, Y.Y. Kang, H. Mok, Platelet-derived nanovesicles for hemostasis without release of pro-inflammatory cytokines, Biomater. Sci. 7 (2019) 856–859.
[37] P. Chen, K. Pan, N. Song, Y. Yang, C. Gu, P. Zhong, L. Li, M. Li, Y. Zhang, Z. Dai, L. Shangguan, C. Lei, Z. Liu, J. Zhang, R. Tang, C. Liu, S. Fan, X. Lin, A natural extracellular matrix hydrogel through selective nutrient restriction for hyperinflammatory starvation therapy, Matter 6 (2023) 397–428.
[38] Z. Dai, C. Xia, T. Zhao, H. Wang, H. Tian, O. Xu, X. Zhu, J. Zhang, P. Chen, Platelet-derived extracellular vesicles ameliorate intervertebral disc degeneration by alleviating mitochondrial dysfunction, Mater Today Bio 18 (2023) 100512.
[39] M. Soleimani, S. Nadri, A protocol for isolation and culture of mesenchymal stem cells from mouse bone marrow, Nat. Protoc. 4 (2009) 102–106.
[40] B. Fang, P. Qiu, C. Xia, D. Cai, C. Zhao, Y. Chen, H. Wang, S. Liu, H. Cheng, Z. Tang, B. Wang, S. Fan, X. Lin, Extracellular matrix scaffold crosslinked with vancomycin for multifunctional antibacterial bone infection therapy, Biomaterials 268 (2021) 120603.
[41] Y. Mu, Y. Zhang, L. Wei, L. Chen, F. Hao, A. Shao, S. Qu, L. Xu, GTKO rabbit: a novel animal model for preclinical assessment of decellularized xenogeneic grafts via in situ implantation, Mater Today Bio 18 (2023) 100505.
[42] J. Hao, B. Bai, Z. Ci, J. Tang, G. Hu, C. Dai, M. Yu, M. Li, W. Zhang, Y. Zhang, W. Ren, Y. Hua, G. Zhou, Large-sized bone defect repair by combining a decalcified bone matrix framework and bone regeneration units based on photo-crosslinkable osteogenic microgels, Bioact. Mater. 14 (2022) 97–109.
[43] G. Lu, Y. Xu, Q. Liu, M. Chen, H. Sun, P. Wang, X. Li, Y. Wang, X. Li, X. Hui, E. Luo, J. Liu, Q. Jiang, J. Liang, Y. Fan, Y. Sun, X. Zhang, An instantly fixable and self-adaptive scaffold for skull regeneration by autologous stem cell recruitment and angiogenesis, Nat. Commun. 13 (2022) 2499.
[44] J. Ye, N. Liu, Z. Li, L. Liu, M. Zheng, X. Wen, N. Wang, Y. Xu, B. Sun, Q. Zhou, Injectable, hierarchically degraded bioactive scaffold for bone regeneration, ACS Appl. Mater. Interfaces 15 (2023) 11458–11473.

[45] K. Liang, C. Zhao, C. Song, L. Zhao, P. Qiu, S. Wang, J. Zhu, Z. Gong, Z. Liu, R. Tang, X. Fang, Y. Zhao, In situ biomimetic mineralization of bone-like hydroxyapatite in hydrogel for the acceleration of bone regeneration, ACS Appl. Mater. Interfaces 15 (2023) 292–308.
[46] A. Grangier, J. Branchu, J. Volatron, M. Piffoux, F. Gazeau, C. Wilhelm, A.K. A. Silva, Technological advances towards extracellular vesicles mass production, Adv. Drug Deliv. Rev. 176 (2021) 113843.
[47] I.D. Pokrovskaya, S. Yadav, A. Rao, E. McBride, J.A. Kamykowski, G. Zhang, M. A. Aronova, R.D. Leapman, B. Storrie, 3D ultrastructural analysis of α-granule, dense granule, mitochondria, and canalicular system arrangement in resting human platelets, Res. Pract. Thromb. Haemost. 4 (2020) 72–85.
[48] A.S. Weyrich, G.A. Zimmerman, Platelets: signaling cells in the immune continuum, Trends Immunol. 25 (2004) 489–495.
[49] U. Moran, R. Phillips, R. Milo, SnapShot: key numbers in biology, Cell 141 (2010) 1262–1262.e1.
[50] Y. Zhang, D. Yi, Q. Hong, J. Cao, X. Geng, J. Liu, C. Xu, M. Cao, C. Chen, S. Xu, Z. Zhang, M. Li, Y. Zhu, N. Peng, Platelet-rich plasma-derived exosomes boost mesenchymal stem cells to promote peripheral nerve regeneration, J. Contr. Release 367 (2024) 265–282.
[51] C. Lin, Y. He, Q. Feng, K. Xu, Z. Chen, B. Tao, X. Li, Z. Xia, H. Jiang, K. Cai, Self-renewal or quiescence? Orchestrating the fate of mesenchymal stem cells by matrix viscoelasticity via PI3K/Akt-CDK1 pathway, Biomaterials 279 (2021) 121235.
[52] J.G. Albeck, G.B. Mills, J.S. Brugge, Frequency-modulated pulses of ERK activity transmit quantitative proliferation signals, Mol Cell. 49 (2013) 249–261.
[53] X. Liang, Y. Ding, F. Lin, Y. Zhang, X. Zhou, Q. Meng, X. Lu, G. Jiang, H. Zhu, Y. Chen, Q. Lian, H. Fan, Z. Liu, Overexpression of ERBB4 rejuvenates aged mesenchymal stem cells and enhances angiogenesis via PI3K/AKT and MAPK/ERK pathways, FASEB J. 33 (2019) 4559–4570.
[54] S.C. Hung, R.R. Pochampally, S.C. Chen, S.C. Hsu, D.J. Prockop, Angiogenic effects of human multipotent stromal cell conditioned medium activate the PI3K-Akt pathway in hypoxic endothelial cells to inhibit apoptosis, increase survival, and stimulate angiogenesis, Stem Cell. 25 (2007) 2363–2370.
[55] Y.Y. Go, C.M. Lee, S.W. Chae, J.J. Song, Regenerative capacity of trophoblast stem cell-derived extracellular vesicles on mesenchymal stem cells, Biomater. Res. 27 (2023) 62.
[56] H. Shindou, T. Shimizu, Acyl-CoA:lysophospholipid acyltransferases, J. Biol. Chem. 284 (2009) 1–5.
[57] J. Aoki, A. Inoue, S. Okudaira, Two pathways for lysophosphatidic acid production, Biochim. Biophys. Acta 1781 (2008) 513–518.
[58] Z. Li, H. Wei, X. Liu, S. Hu, X. Cong, X. Chen, LPA rescues ER stress-associated apoptosis in hypoxia and serum deprivation-stimulated mesenchymal stem cells, J. Cell. Biochem. 111 (2010) 811–820.
[59] L. Badri, V.N. Lama, Lysophosphatidic acid induces migration of human lung-resident mesenchymal stem cells through the β-catenin pathway, Stem Cell. 30 (2012) 2010–2019.
[60] D. Yasuda, D. Kobayashi, N. Akahoshi, T. Ohto-Nakanishi, K. Yoshioka, Y. Takuwa, S. Mizuno, S. Takahashi, S. Ishii, Lysophosphatidic acid-induced YAP/TAZ activation promotes developmental angiogenesis by repressing Notch ligand Dll4, J. Clin. Investig. 129 (2019) 4332–4349.
[61] K. Kano, J. Aoki, T. Hla, Lysophospholipid mediators in health and disease, Annu. Rev. Pathol. 17 (2022) 459–483.
[62] Y.C. Yung, N.C. Stoddard, J. Chun, LPA receptor signaling: pharmacology, physiology, and pathophysiology, J. Lipid Res. 55 (2014) 1192–1214.
[63] H.B. Hu, Z.Q. Song, G.P. Song, S. Li, H.Q. Tu, M. Wu, Y.C. Zhang, J.F. Yuan, T.T. Li, P.Y. Li, Y.L. Xu, X.L. Shen, Q.Y. Han, A.L. Li, T. Zhou, J. Chun, X.M. Zhang, H.Y. Li, LPA signaling acts as a cell-extrinsic mechanism to initiate cilia disassembly and promote neurogenesis, Nat. Commun. 12 (2021) 662.
[64] Z. Peng, Y. Chang, J. Fan, W. Ji, C. Su, Phospholipase A2 superfamily in cancer, Cancer Lett. 497 (2021) 165–177.
[65] M. Murakami, The phospholipase A(2) superfamily as a central hub of bioactive lipids and beyond, Pharmacol. Ther. 244 (2023) 108382.
[66] J.E. Barthold, B.M. Martin, S.L. Sridhar, F. Vernerey, S.E. Schneider, A. Wacquez, V. Ferguson, S. Calve, C.P. Neu, Recellularization and integration of dense extracellular matrix by percolation of tissue microparticles, Adv. Funct. Mater. 31 (2021).
[67] T. Novak, B. Seelbinder, C.M. Twitchell, S.L.P. Voytik-Harbin, C.P.P. Neu, Dissociated and reconstituted cartilage microparticles in densified collagen induce local hMSC differentiation, Adv. Funct. Mater. 26 (2016) 5427–5436.
[68] N. Huebsch, E. Lippens, K. Lee, M. Mehta, S.T. Koshy, M.C. Darnell, R.M. Desai, C. M. Madl, M. Xu, X. Zhao, O. Chaudhuri, C. Verbeke, W.S. Kim, K. Alim, A. Mammoto, D.E. Ingber, G.N. Duda, D.J. Mooney, Matrix elasticity of void-forming hydrogels controls transplanted-stem-cell-mediated bone formation, Nat. Mater. 14 (2015) 1269–1277.
[69] M. Li, Y. Yu, K. Xue, J. Li, G. Son, J. Wang, W. Qian, S. Wang, J. Zheng, C. Yang, J. Ge, Genistein mitigates senescence of bone marrow mesenchymal stem cells via ERRα-mediated mitochondrial biogenesis and mitophagy in ovariectomized rats, Redox Biol. 61 (2023) 102649.
[70] J. Yang, L. Xiao, L. Zhang, G. Luo, Y. Ma, X. Wang, Y. Zhang, Platelets: A Potential Factor that Offers Strategies for Promoting Bone Regeneration, Tissue Eng., Part B (2024).
[71] R. Gruber, How to explain the beneficial effects of platelet-rich plasma, Periodontol 2000 (2024).
[72] T. Spakova, J. Janockova, J. Rosocha, Characterization and therapeutic use of extracellular vesicles derived from platelets, Int. J. Mol. Sci. 22 (1) (2021) Scheme.